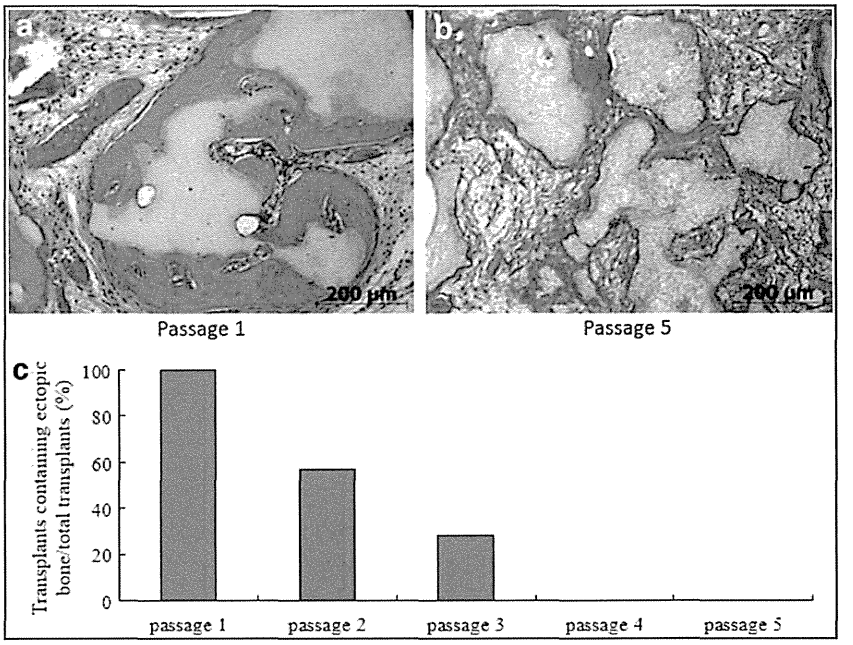

FIG. 1. Effect of passage number on ectopic *in vivo* osteogenic ability. Upper panels showing ectopic bone formation at the back of nude mice with tissue-engineered bone using passage 1 (**a**) and passage 5 (**b**) human bone marrow stromal cells (BMSCs). The success of ectopic bone formation quickly decrease after passage and no bone formation was observed after passage 4 (**c**). Note that the ability is quickly lost during passage. Modified from Agata *et al.*[7] Color images available online at www.liebertpub.com/teb

shown that basic fibroblast growth factor (bFGF) is beneficial to maintain *in vivo* osteogenic ability of BMSCs.[7]

Clinical Studies on Alveolar Bone Tissue Engineering

The results from clinical studies on alveolar bone tissue engineering using BMSCs were first reported in 2004. In this study, bone marrow-derived MSCs were mixed with platelet-rich plasma as a scaffold.[8] Bone regeneration was observed in all moderate atrophy cases. Another clinical study utilized BMSCs and hydroxyapatite granules. BMSCs were induced into osteogenic cells for 1 week and transplanted. In this study, bone formation was observed in three cases, but there was no apparent bone formation from the

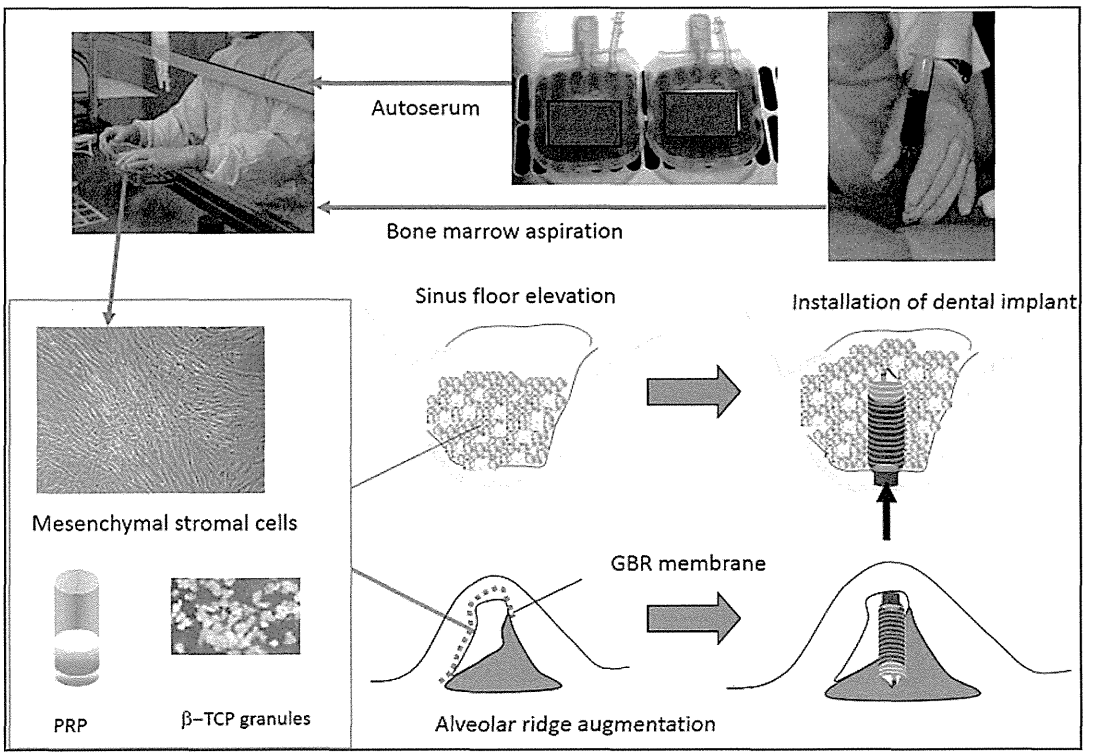

FIG. 2. The procedure for clinical study of alveolar bone regeneration at IMSUT Hospital, The Institute of Medical Science, The University of Tokyo. β-TCP, beta-tricalcium phosphate; PRP, platelet rich plasma. Color images available online at www.liebertpub.com/teb

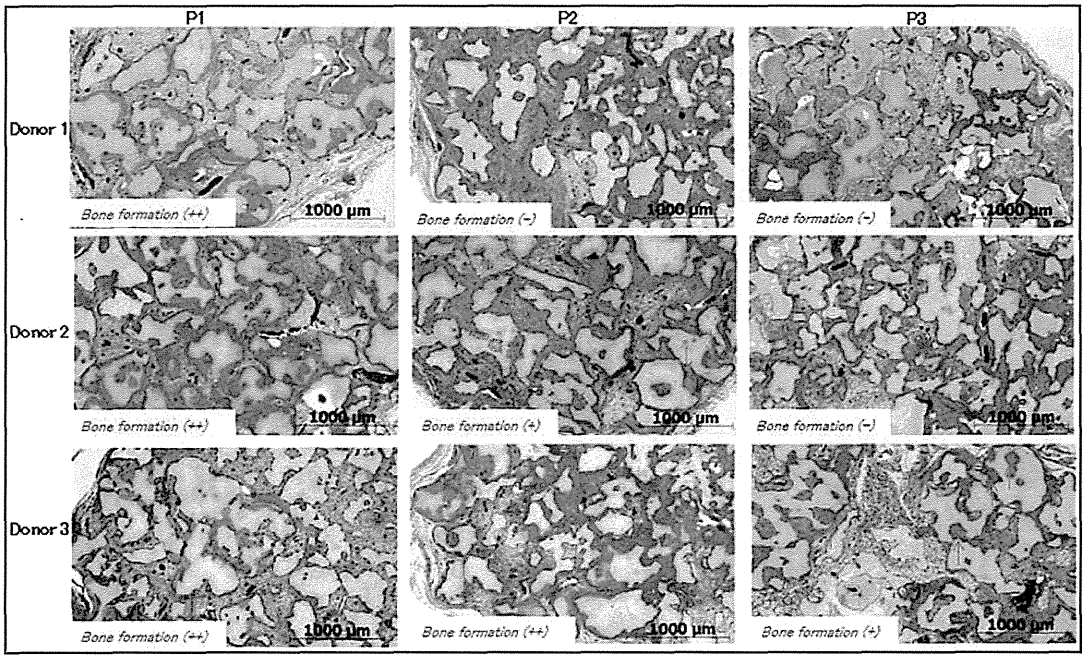

FIG. 3. Individual (donor) variations of *in vivo* osteogenic ability and their changes during passage. Note that the effect of passage differed between individuals. Modified from Agata.[9] Color images available online at www.liebertpub.com/teb

transplanted cells in cases where the atrophy was severe. Thus, the efficacy of clinical alveolar bone tissue engineering for severe atrophy cases remains controversial.

We have conducted a clinical study of bone tissue engineering for severe atrophy of alveolar bone. In this study, autologous BMSCs were transplanted together with platelet-rich plasma gel and beta-tricalcium phosphate (β-TCP) granules as scaffolds (Fig. 2). The results from a 2-year observation showed that bone regeneration was observed in all patients, although significant individual variations in cell growth, differentiation, and levels of bone regeneration were observed (Asahina *et al.*, manuscript in preparation). This type of study, focused on severe atrophy cases, may prove the usefulness of alveolar bone tissue engineering. In terms of safety, no side effects or related complications have been reported, which may imply the relatively safety nature of alveolar bone tissue engineering using BMSCs.

Toward the Establishment of Reliable Alveolar Bone Tissue Engineering Using BMSCs

Although clinical studies have confirmed the feasibility and safety of alveolar bone tissue engineering using BMSCs, one of the important clinical benchmarks is the efficacy for severe atrophy cases. The results from focused studies with selected cases will provide the evidence. Another important problem is the individual variation as shown by basic and preliminary clinical studies. Since the shape and the size of bone defect vary among individuals, it might be impossible to completely eliminate such variations. Accordingly, it should be important to minimize the variation in other factors, such as cells. In terms for BMSCs, there was no significant difference in the expression of mesenchymal stem cell markers during passage.[7] In contrast, a large variation was observed in the *in vivo* bone forming ability among donors and during passage (Fig. 3).[7,8,9] We believe the usage of early passage cells as well as growth factors (bFGF) may minimize the variation, which should be tested under clinical settings.

In spite of the number of studies and the clinical efficacy of bone tissue engineering, it is not a standard treatment at present. It is necessary to show the superiority of clinical outcome compared with standard autologous bone transplantation and allogenic (or xenogenic) transplantation. Furthermore, tissue engineering requires special facility for cell culture and there is a requirement for many safety examinations, which may also increase the cost for treatment. Those technologies, which may support the widespread use of bone tissue engineering, should be investigated.

Tissue engineering is one of the most rapidly progressing fields and alveolar bone is still an attractive target for tissue engineering.[10] The application of bone tissue engineering is not limited for dental implants and is successfully applied for other diseases such as nonunion fractures[11] and alveolar clefts.[12,13]

Disclosure Statement

No competing financial interests exist.

References

1. Jensen, S.S., and Terheyden, H. Bone augmentation procedures in localized defects in the alveolar ridge: clinical results with different bone grafts and bone-substitute materials. Int J Oral Maxillofac Implants **24 Suppl,** 218, 2009.
2. Clavero, J., and Lundgren, S. Ramus or chin grafts for maxillary sinus inlay and local onlay augmentation: comparison of donor site morbidity and complications. Clin Implant Dent Relat Res **5,** 154, 2003.

3. Becker, W., Urist, M., Becker, B.E., Jackson, W., Parry, D.A., Bartold, M., Vincenzzi, G., De Georges, D., and Niederwanger, M. Clinical and histologic observations of sites implanted with intraoral autologous bone grafts or allografts. 15 human case reports. J Periodontol **67,** 1025, 1996.
4. Quatro, R., Mastrogiacomo, M., and Cancedda, R. Repair of large bone defects with the use of autologous bone marrow stromal cells. N Engl J Med **344,** 385, 2001.
5. Yamada, Y., Ueda, M., Hibi, H., and Nagasaka, T. Translational research for injectable tissue-engineered bone regeneration using mesenchymal stem cells and platelet-rich plasma: from basic research to clinical case study. Cell Transplant **13,** 343, 2004.
6. Meijer, G.J., de Bruijn, J.D., Koole, R., and van Blitterswijk, C.A. Cell based bone tissue engineering in jaw defects. Biomaterials **29,** 3053, 2008.
7. Agata, H., Asahina, I., Watanabe, N., Ishii, Y., Kubo, N., Ohshima, S., Yamazaki, M., Tojo, A., and Kagami, H. Characteristic change and loss of *in vivo* osteogenic abilities of human bone marrow stromal cells during passage. Tissue Eng Part A **16,** 663, 2010.
8. Sugiura, F., Kitoh, H., and Ishiguro, N. Osteogenic potential of rat mesenchymal stem cells after several passages. Biochem Biophys Res Commun **316,** 233, 2004.
9. Agata, H. Toward establishment of truly reliable protocol for bone tissue Engineering. Regenerative Medicine, **8,** 439, 2009. (In Japanese).
10. Egusa, H., Sonoyama, W., Nishimura, M., Atsuta, I., and Akiyama, K. Stem cells in dentistry—Part II: clinical applications. J Prosthodont Res **56,** 229, 2012.
11. Shoji, T., Ii, M., Mifune, Y., Matsumoto, T., Kawamoto, A., Kwon, S.M., Kuroda, T., Kuroda, R., Kurosaka, M., and Asahara, T. Local transplantation of human multipotent adipose-derived stem cells accelerates fracture healing via enhanced osteogenesis and angiogenesis. Lab Invest **90,** 637, 2010.
12. Pradel, W., and Lauer, G. Tissue-engineered bone grafts for osteoplasty in patients with cleft alveolus. Ann Anat **194,** 545, 2012.
13. Janssen, N.G., Weijs, W.L., Koole, R., Rosenberg, A.J., and Meijer, G.J. Tissue engineering strategies for alveolar cleft reconstruction: a systematic review of the literature. Clin Oral Investig **18,** 219, 2014.

Address correspondence to:
Hideaki Kagami, DDS, PhD
Tissue Engineering Research Group
Division of Molecular Therapy
The Advanced Clinical Research Center
The Institute of Medical Science
The University of Tokyo
4-6-1 Shirokanedai
Minato-ku
Tokyo 108-8639
Japan

E-mail: kagami@ims.u-tokyo.ac.jp

Received: September 15, 2013
Accepted: January 30, 2014
Online Publication Date: March 5, 2014

Hindawi Publishing Corporation
Stem Cells International
Volume 2014, Article ID 101349, 8 pages
http://dx.doi.org/10.1155/2014/101349

Research Article

DNA Methylation Is Involved in the Expression of miR-142-3p in Fibroblasts and Induced Pluripotent Stem Cells

Siti Razila Abdul Razak,[1] Yukihiro Baba,[1] Hiromitsu Nakauchi,[2] Makoto Otsu,[2] and Sumiko Watanabe[1]

[1]*Division of Molecular and Developmental Biology, Institute of Medical Science, University of Tokyo, 4-6-1 Shirokanedai, Minato-ku, Tokyo 108-8639, Japan*
[2]*Division of Stem Cell Therapy, Center for Stem Cell Biology and Regenerative Medicine, Institute of Medical Science, University of Tokyo, 4-6-1 Shirokanedai, Minato-ku, Tokyo 108-8639, Japan*

Correspondence should be addressed to Sumiko Watanabe; sumiko@ims.u-tokyo.ac.jp

Received 11 August 2014; Revised 4 November 2014; Accepted 14 November 2014; Published 2 December 2014

Academic Editor: Chia-Lin Wei

MicroRNAs are differentially expressed in cells and regulate multiple biological processes. We have been analyzing comprehensive expression patterns of microRNA in human and mouse embryonic stem and induced pluripotent stem cells. We determined microRNAs specifically expressed in these pluripotent stem cells, and miR-142-3p is one of such microRNAs. miR-142-3p is expressed at higher levels in induced pluripotent stem cells relative to fibroblasts in mice. Level of expression of miR142-3p decreased during embryoid body formation from induced pluripotent stem cells. Loss-of-function analyses of miR-142-3p suggested that miR-142-3p plays roles in the proliferation and differentiation of induced pluripotent stem cells. CpG motifs were found in the 5′ genomic region of the *miR-142-3p*; they were highly methylated in fibroblasts, but not in undifferentiated induced pluripotent stem cells. Treating fibroblasts with 5-aza-2′-deoxycytidine increased the expression of miR-142-3p significantly and reduced methylation at the CpG sites, suggesting that the expression of miR-142-3p is suppressed by DNA methylation in fibroblasts. Luciferase analysis using various lengths of the 5′ genomic region of miR142-3p indicated that CpGs in the proximal enhancer region may play roles in suppressing the expression of miR-142-3p in fibroblasts.

1. Introduction

The self-renewal and differentiation of pluripotent stem cells are regulated by various factors including growth factors, cytokines, intracellular signaling molecules, the extracellular matrix, and transcription factors. In addition, the roles of microRNAs (miRNAs) and epigenetic regulation such as DNA methylation and histone modification have received increasing attention in recent years [1]. The complex regulatory networks involving these mechanisms have been studied extensively in embryonic stem (ES) and induced pluripotent stem (iPS) cells and have revealed that the regulatory activity, in combination with transcription factors, is associated with pluripotency [2].

We previously assessed the expression pattern of miRNAs in human and mouse ES and iPS cells [3]. We found that several miRNAs were highly expressed in undifferentiated iPS cells [3]. Among these, we focused on miRNA- (miR-) 142-3p in the current study. miR-142 was first identified in hematopoietic cells [4], where it plays various roles in differentiation and functions during hemopoiesis [5–7]. miR-142 is highly conserved among vertebrates [8] and has been implicated in cardiac cell fate determination [9], osteoblast differentiation [10], and vascular development [11]. In cancer, *miR-142-3p* was identified at the breakpoint of a *MYC* translocation in B-cell leukemia [12] and was mutated in 20% of diffuse large B-cell lymphomas [13]. It is also critically involved in T-cell leukemogenesis [14] and the migration of hepatocellular carcinoma cells [15].

miRNAs are transcribed by RNA polymerase II [16], which involves various transcription factors. In hematopoietic cells, specifically, Spi1, Cebpb, Runx1, and LMO2 have

all been reported to regulate miR-142 expression [17, 18]. However, these transcription factors are mostly hematopoietic cell-specific, suggesting that the expression of miR-142 in undifferentiated iPS cells involves regulation of other factors. In this study, we examined the roles of miR-142-3p in iPS cells and found that miR-142-3p might be involved in the proliferation of iPS cells and in maintaining their immaturity. Furthermore, miR-142-3p might also play roles in the mesodermal differentiation of iPS cells. Our data suggest roles for the methylation of CpG motifs in the 5′ genomic region of miR-142-3p in suppressing its expression in fibroblasts. Luciferase analysis of the isolated genomic region of miR-142-3p supports the idea that the expression of miR-142-3p in cells including fibroblasts and iPS is regulated, at least partially, by DNA methylation.

2. Materials and Methods

2.1. Cell Lines, 5-Aza-2′-deoxycytidine (5-Aza-dC) Treatment, and Transfection. 3T3 cells were cultured in the DMEM (Nacalai Tesque) supplemented with 10% fetal bovine serum (GIBCO) and 0.5% penicillin/streptomycin (Nacalai Tesque). Preparation and culture of mouse embryonic fibroblast (MEF) and tail-tip fibroblasts (TTF) are described previously [3]. ICR mice were purchased from local dealers, and all experiments with animals were approved by the Animal Care Committee of the Institute of Medical Science at the University of Tokyo. Mouse iPS cell line, SP-iPS, was from B6 mouse MEF with infection of 4 factors (Sox2, Oct3/4, Klf4, and c-myc) by using retrovirus [19]. Culture of the iPS cells and formation of embryoid body (EB) is described previously [3]. For treatment of 5-aza-dC, cells were treated with final concentration of 5 or 10 μM 5-aza-dC (SIGMA) or dimethyl sulfoxide (DMSO) for control samples 6 hours after the cells were plated, and cells were cultured for 3 days before analysis unless otherwise noted. For plasmid transfection, 3T3 cells were plated in a 24-well culture plate 1 day before transfection. Transfection of luciferase plasmid was done by using Gene Juice Transfection Reagent (Novagen). Briefly, Gene Juice Reagent (1.5 μL), plasmid (0.25 μg in 0.25 μL for each plasmid), and Opti-MEM (Gibco-Life Technologies) were mixed and added to 3T3 cells. For plasmid transfection to iPS, electroporation was employed. iPS cells were dissociated into single cells by 0.05% trypsin-EDTA, washed with PBS, and resuspended in Opti-MEM. For each transfection, 1×10^6 cells/30 μL were gently mixed with 15 μg of plasmid and placed in 2 mm gap electroporation cuvette (Nepa Gene Co., Ltd.). The cells were electroporated for two times at 175 V, 2 ms at 50 ms interval (CUY21 EDIT, Nepa Gene Co., Ltd). Immediately after electroporation, 1 mL of iPS culture medium was gently added to the cuvette, and cells were transferred and cultured on feeder cells in iPS medium. On the following day, the cells were dissociated and stained with SSEA-1 marker. Subsequently, the GFP + SSEA-1 + double positive cells from study or control group were sorted by FACS (MoFlo, DakoCytomation) and used for cell proliferation and colony formation assay.

2.2. RNA Extraction and Real-Time PCR for Quantification of miRNAs and mRNA. Total RNA was extracted using the Sepasol (Nacalai Tesque), and level of mature miRNAs was detected using TaqMan MicroRNA systems (Applied Biosystems) using primer specific for each mature miRNA supplied by Applied Biosystems using Light Cycler 1.5 (ROCHE). Briefly, a total of 500 ng RNA were reverse-transcribed with Taqman Reverse-Transcription PCR Kit with specific primer for miR-142-3p. Then, cDNA was mixed with TaqMan Universal Master Mix (Applied Biosystems) and was subjected for real-time PCR. Ct value was analyzed with SDS 2.4 and RQmanager 1.2.1 and quantitated using $2^{-\Delta\Delta Ct}$ method (Livak, 2001). All data were normalized to endogenous control, the U6 snRNA. Sequences of the primers are T/brachyury 5′-cacaccactgacgcacacggt-3′, 5′-atgaggaggctttgggccgt-3′, Gata4 5′-agccggtgggtgatccgaag-3′, 5′-agaaatcgtgcgggagggcg-3′, Fgf5 5′-gcagtccgagcaaccggaact-3′, and 5′-ggacttctgcgaggctgcga-3′. For quantification of mRNA, total RNA (1 μg) from each sample was used to generate cDNA using ReverTra Ace qRT-PCR RT Kit (Toyobo). Then, cDNA was mixed with Sybr Green Master Mix (ROCHE) and was subjected for real-time PCR using Light Cycler 1.5 (ROCHE). Expression levels of mRNA were compared to known standard samples and normalized to GAPDH.

2.3. Isolation and Bisulfite Treatment of Genomic DNA. Genomic DNA was isolated from ~5×10^6 cells using the QIAamp DNA Mini and Blood Mini kit (Qiagen). Genomic DNA (1 μg) was subjected for bisulfite conversion using EpiTect Bisulfite (Qiagen). The converted DNA was further subjected to PCR for A-tailing procedure with HotStarTaq DNA Polymerase (Qiagen). Regions covering up to 700 bp upstream of the miR-142 seed sequence were amplified and were cloned into pGEM-T Easy Vector (Invitrogen). All positive clones were sequence and methylation results obtained were analyzed by Quantification Tool for Methylation Analysis (QUMA, http://quma.cdb.riken.jp) which was used for detection of CpG island methylation [20].

2.3.1. DNA Construction. Plasmids containing antisense sequences of mature miR-142-3p or miR-17 expression plasmid were constructed as follows: double strand DNA, which encode antisense of mature miR-142-3p or miR-17, was inserted downstream of U6 promoter using *Bam*HI and *Eco*RI sites of pMX retrovirus vector containing EGFP after 5′ LTR (Figure 1(b)). Expression plasmids for mouse Oct4, Sox2, Klf, and Myc were purchased from AddGene.

2.3.2. Cell Sorting, Cell Staining with Alkaline Phosphatase (ALP), and Immunostaining. Cells' sorting was done using a MoFlo (DakoCytomation). ALP staining was done using BCIP-NBT solution kit for alkaline phosphatase stain (Nacalai Tesque) according to the manufacturer's instructions. Immunostaining was done using antibody anti-Ki67 proliferation antigen (BD Biosciences), and the primary antibody was visualized using appropriate secondary antibody conjugated with Alexa 488 (Molecular Probes).

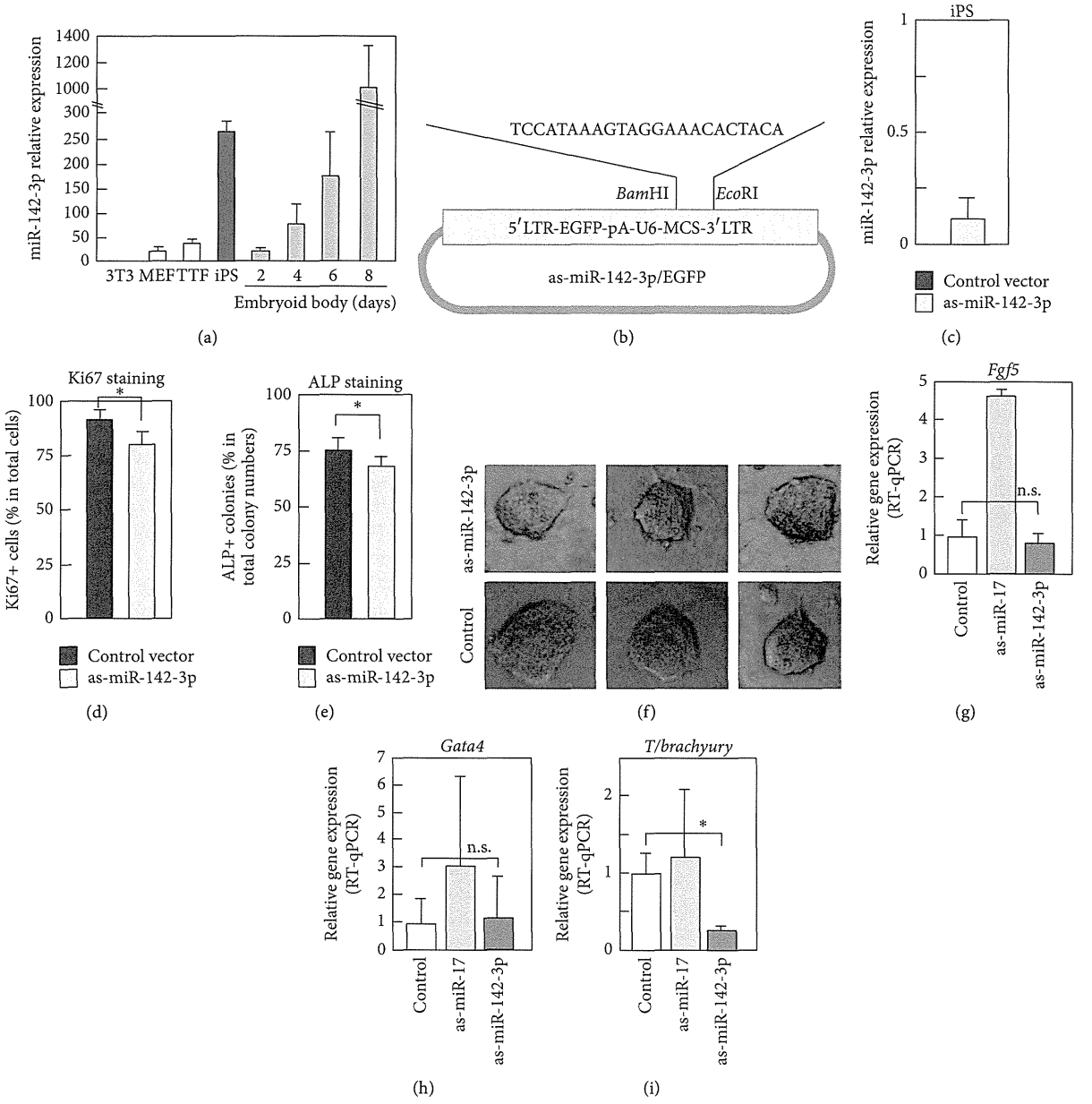

FIGURE 1: Differential expression level of miR-142-3p in fibroblasts and iPS. (a) Expression of miR-142-3p was examined by RT-qPCR in various cells. Total RNA was extracted from indicated cells, and RT-qPCR was done using TaqMan MicroRNA systems. U6 shRNA was used as a control. Experiments were done three times using independently prepared cells, and average values with standard deviation are shown. (b) Schematic representation of antisense- (as-) miR-142-3p and EGFP expression plasmid. LTR was used to drive EGFP, and U6 promoter was used to drive as-miR-142-3p. (c) Effect of overexpressed as-miR-142-3p for expression level of endogenous miR-142-3p in iPS cells. as-miR-142-3p/EGFP or control vector was transfected into iPS, and, after 24 hours, level of miR-142-3p in iPS was examined by RT-qPCR. Data were expressed as relative expression level of miR-142-3p in as-miR-142-3p/EGFP expressing cells to that in control vector expressing cells. Experiments were performed three times, and average values with standard deviation are shown. (d, e, and f) Effects of expression of as-miR-142-3p for proliferation and alkaline phosphatase (ALP) expression of iPS. as-miR-142-3p/EGFP plasmid was transfected into undifferentiated iPS, and EGFP positive cells were purified by a cell sorter. Then EGFP positive cells were cultured for 2 days for Ki67 immunostaining and for 5 days for ALP assay. Immunostaining with anti-Ki67 antibody or ALP staining was done, and positive cells were counted under a microscope. Experiments were performed three times, and average values with standard deviation are shown. In (f), morphology of representative colonies of as-miR-142-3p or control vector transfected iPS is shown. (g–i) Expression of lineage marker genes in embryoid body (EB). iPS cells were transfected with as-miR-142-3p/EGFP or as-miR-17/EGFP as a control, purified according to their expression of EGFP, and then subjected to an EB formation. After 6 days of culturing in EB formation condition, the differentiation of cells into the ectodermal (g), endodermal (h), and mesodermal (i) lineages was assessed using RT-qPCR with primers against *Fgf5*, *Gata4*, and *T brachyury*, respectively. P value, $* < 0.05$ and n.s. > 0.05, was calculated by Student's t-test.

2.3.3. Luciferase Analysis. 3T3 cells were plated in a 24-well culture plate 1 day before transfection and transfected with luciferase plasmid (0.25 μg) by using Gene Juice Transfection Reagent (Novagen). Six hours after transfection, cells were treated with final concentration of 10 μM of 5-azacytidine and were cultured for 3 days. Cells were harvested using Cell Culture Lysis Reagent 5X (Promega). Luciferase activity toward a luciferase assay substrate (Promega) was measured with a luminometer (Lumat LB9507, Berthold Technologies).

3. Results

3.1. Characterization of miR-142-3p Expression in iPS Cells, Embryoid Bodies, and Fibroblasts. We previously characterized the expression pattern of miRNAs in mouse and human iPS and ES cells using miRNA arrays and found that miR-142-3p, but not miR-142-5p, was expressed at high levels in iPS cells (see Supplementary Figure 1 available online at http://dx.doi.org/10.1155/2014/101349) [3]. We first confirmed the expression pattern of miR-142-3p using quantitative reverse transcription-polymerase chain reaction (qRT-PCR). miR-142-3p was expressed at a high level in undifferentiated iPS cells, whereas fibroblasts such as 3T3, mouse embryonic fibroblasts (MEFs), and tail-tip fibroblasts (TTF) expressed only very low levels (Figure 1(a)). When iPS cells were differentiated by formation of embryoid bodies (EBs), the expression of miR-142-3p fell to very low levels on day 2 but then increased on the following days (Figure 1(a)).

3.1.1. Functional Analyses of miR-142-3p in iPS Cell Physiology. We next constructed an expression plasmid encoding antisense miR-142-3p (as-miR-142-3p) and enhanced green fluorescent protein (EGFP; Figure 1(b)). A plasmid without insertion of antisense miR-142-3p was used as a control for all experiments. The effect of expressing as-miR-142-3p on endogenous miR-142-3p was then examined and confirmed in mouse iPS cells (Figure 1(c)). Specifically, as-miR-142-3p/EGFP was transfected into undifferentiated iPS to analyze the role of miR-142-3p in the proliferation and maintenance of immaturity in iPS cells. Twenty-four hours after transfection, EGFP-positive cells were purified using a cell sorter and cultured for 3 days. Cell proliferation was then assessed by immunostaining for Ki67, a proliferative marker (Figure 1(d)). The population of Ki67-positive cells was slightly, but significantly, lower in as-miR-142-3p-expressing iPS cells (Figure 1(d)). We then counted the number of alkaline phosphatase- (ALP-) positive iPS colonies, and significantly fewer ALP-positive cells were found within the as-miR-142-3p-expressing iPS colonies (Figure 1(e)). Morphology of colonies of iPS cell was indistinguishable between control and as-miR-142-3p expressing samples (Figure 1(f)).

We then analyzed the roles of miRNA-142-3p on the ability of iPS cells to differentiate. iPS cells were transfected with as-miR-142-3p/EGFP, purified according to their expression of EGFP, and then subjected to an EB formation assay. An expression plasmid containing antisense sequence against miR-17, which is expressed at very high levels in undifferentiated iPS cells [3, 21], was used as a control. After 6 days, the differentiation of cells into the ectodermal, endodermal, and mesodermal lineages was assessed using real-time quantitative PCR (qPCR) with primers against *Fgf5*, *Gata4*, and *T brachyury*, respectively (Figures 1(g), 1(h), and 1(i)). Data revealed that as-miR-142-3p, but not as-miR-17, suppressed the expression of *T brachyury*, which is expressed specifically in cells of the mesodermal lineage [22] (Figure 1(i)). The expression of as-miR-142-3p did not affect the expression of *Fgf5* or *Gata4*, although as-miR-17 enhanced expression of *Fgf5*, as expected (Figures 1(g) and 1(h)).

3.2. 5-Aza-2′-deoxycytidine Treatment Upregulates miR-142-3p in Fibroblasts. To assess the transcriptional regulation of miR-142-3p expression, we examined its 5′ genomic sequence and identified 25 CpG motifs in a region covering ~1000 base pairs (bp) upstream of the miR-142-5p core sequence (Supplementary Figure 2). We hypothesized that miR-142-3p expression is regulated epigenetically by DNA methylation in iPS cells and fibroblasts. MEFs and 3T3 cells were treated for 3 days with 5 or 10 μM of 5-aza-2′-deoxycytidine (5-aza-dC), a DNA methyltransferase inhibitor (Dnmt), and the levels of miR-142-3p were assessed using real-time qPCR. The expression of miR-142-3p was upregulated by 5-aza-dC treatment (Figures 2(a) and 2(b)). In contrast, the levels of miR-17 were rather reduced but not significantly by 5-aza-dC (Figure 2(c)), whereas the expression of neither miR-142-3p nor miR-17 was changed significantly by 5-aza-dC in undifferentiated iPS cells (Figures 2(d) and 2(e)). We also examined the effects of 5-aza-dC on miR-142-3p in EBs and found that 10 μM 5-aza-dC rather suppressed the expression (Figure 2(f)). We also examined the effects of 5-aza-dC for miR-142-3p expression in thymocytes. Levels of miR-142-3p were upregulated slightly by 10 μM of 5-aza-dC, but to a much lesser extent than observed in fibroblasts (Figure 2(g)). Taken together, these results suggest that miR-142-3p is suppressed by DNA methylation in fibroblasts but that the downregulation of miR-142-3p during EB formation might be regulated by a different mechanism.

3.3. Proximal CpGs in the miR-142-3p Genomic Region Regulate Transcriptional Activity. We next performed promoter analyses of different fragments of the 5′ upstream region of miR-142-3p using luciferase assays. Previous reports indicated that transiently transfected plasmids could be CpG-methylated in the cells *de novo* [23, 24]. Luciferase constructs were transfected into 3T3 cells, which were cultured in the presence or absence of 5-aza-dC for 3 days. Luciferase assays were then performed. In the absence of 5-aza-dC, the −274, −540, and −860 Luc constructs showed significant luciferase activity, which increased gradually when longer promoters were used (Figure 3(a)). In contrast, −1130 Luc had very low luciferase activity, suggesting the presence of a region between −860 and −1130 nucleotides (nt) that inhibited luciferase activity. When cells were cultured in the presence of 5-aza-dC, the luciferase activity of −274 Luc was upregulated significantly (Figure 3(a)). Since there are six CpGs in the region covering −274 to ATG, we speculated that

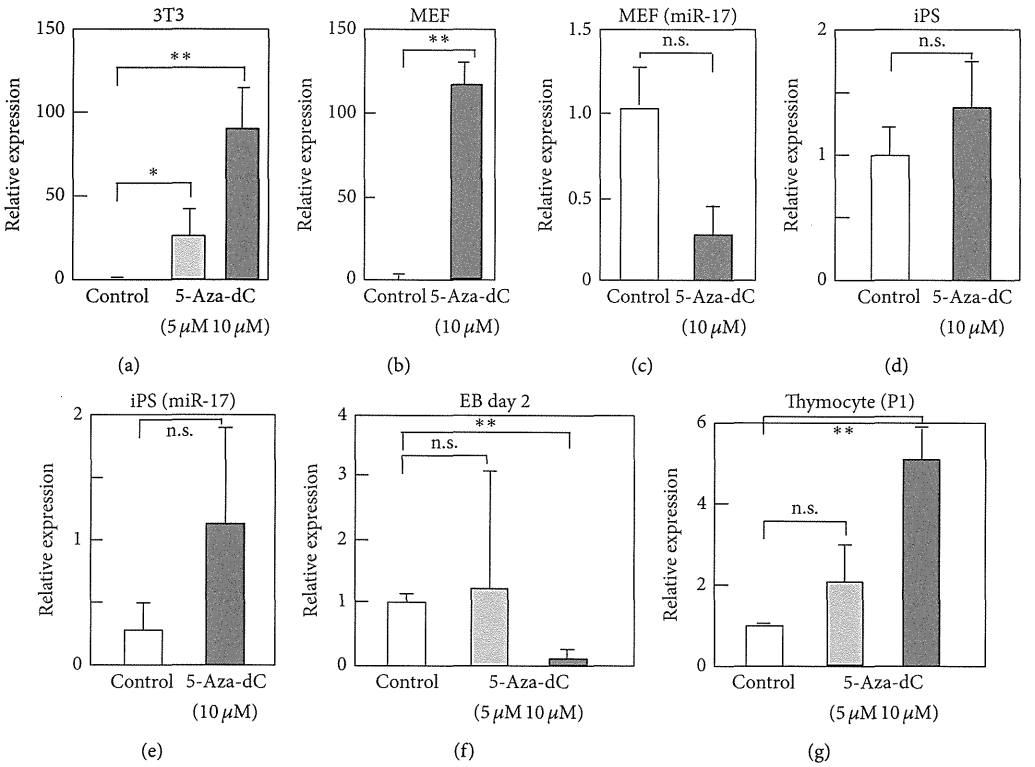

FIGURE 2: 5-Aza-2′-deoxycytidine (5-aza-dC) treatment upregulates miR-142-3p in fibroblasts. (a–g) 3T3 (a), MEF (b, c), iPS (d, e), embryoid body (EB) formed from mouse iPS (f), or mouse thymocytes (g) were treated with 5-aza-dC at indicated final concentration (5 or 10 μM). Cells were cultured for 3 days in the presence of 5-aza-dC, except for EB, which was treated with 5-aza-dC for two days. Control cells were treated with DMSO. Then, cells were harvested, and total RNA was extracted. Level of miR-142-3p or miR-17 was examined by RT-qPCR. Value of U6 was used as a control. Values are expressed as relative to those of control samples of each cell type and are average of 3 or 4 times experiments with standard deviation. P value, $** < 0.01$, $0.01 < * < 0.05$, and n.s. > 0.05, was calculated by Student's t-test.

the methylation status of the proximal six CpGs might play roles in the upregulation of luciferase activity.

3.4. CpG Methylation in the 5′ Genomic Region of miR-142-3p. To further elucidate the role of CpG sites and DNA methylation in regulating the expression of miR-142-3p, we analyzed the methylation status of the CpG sites identified in the region up to 700 bp upstream of the pre-miR-142-5p core region (Supplementary Figure 2) using bisulfite conversion. Analyses performed in 3T3 cells and MEFs revealed that the CpG sites were hypermethylated (Figures 3(b) and 3(c)). In contrast, those in undifferentiated iPS cells were hypomethylated (Figure 3(d)). We then analyzed the effects of 5-aza-dC on the methylation status in 3T3 cells and MEFs. Treatment with 5-aza-dC lowered methylation levels significantly, particularly at the proximal eight CpGs (Figures 3(e) and 3(f)). CpGs were also hypomethylated in day 5 EBs (Figure 3(g)), even though the expression of miR-142-3p was much lower than in undifferentiated iPS cells (Figure 1(a)).

3.5. Roles of Pluripotency-Related Transcription Factors in miR-142-3p Gene Activation. We next investigated the possible involvement of the pluripotency-associated transcription factors Oct4, Sox2, Klf4, and c-Myc in the regulation of miR-142-3p transcription. The miR-142-3p promoter-luciferase construct (−540 Luc) was transfected into 3T3 cells with one of the four transcription factors, and luciferase assays were performed 3 days later. Luciferase activity was strongly upregulated by Klf4, whereas the other three transcription factors suppressed luciferase activity (Figure 3(h)). In addition, cotransfection with Klf4 and one of Oct4, Sox2, and c-Myc lowered luciferase activity compared with Klf4 alone (Figure 3(h)). We then analyzed the effects of overexpressing these transcription factors on the expression of endogenous miR-142-3p in 3T3 cells, but no effects were observed (Figure 3(i)).

4. Discussion

This study revealed that miR-142-3p is expressed in undifferentiated iPS cells, but not in fibroblasts, and DNA methylation might play a pivotal role in suppressing miR-142-3p expression in fibroblasts. Previous studies revealed that the transcription of miRNAs could be regulated by DNA methylation [25, 26]. miR-142-3p was reported to be upregulated in the human melanoma cell line WM1552C after treatment with

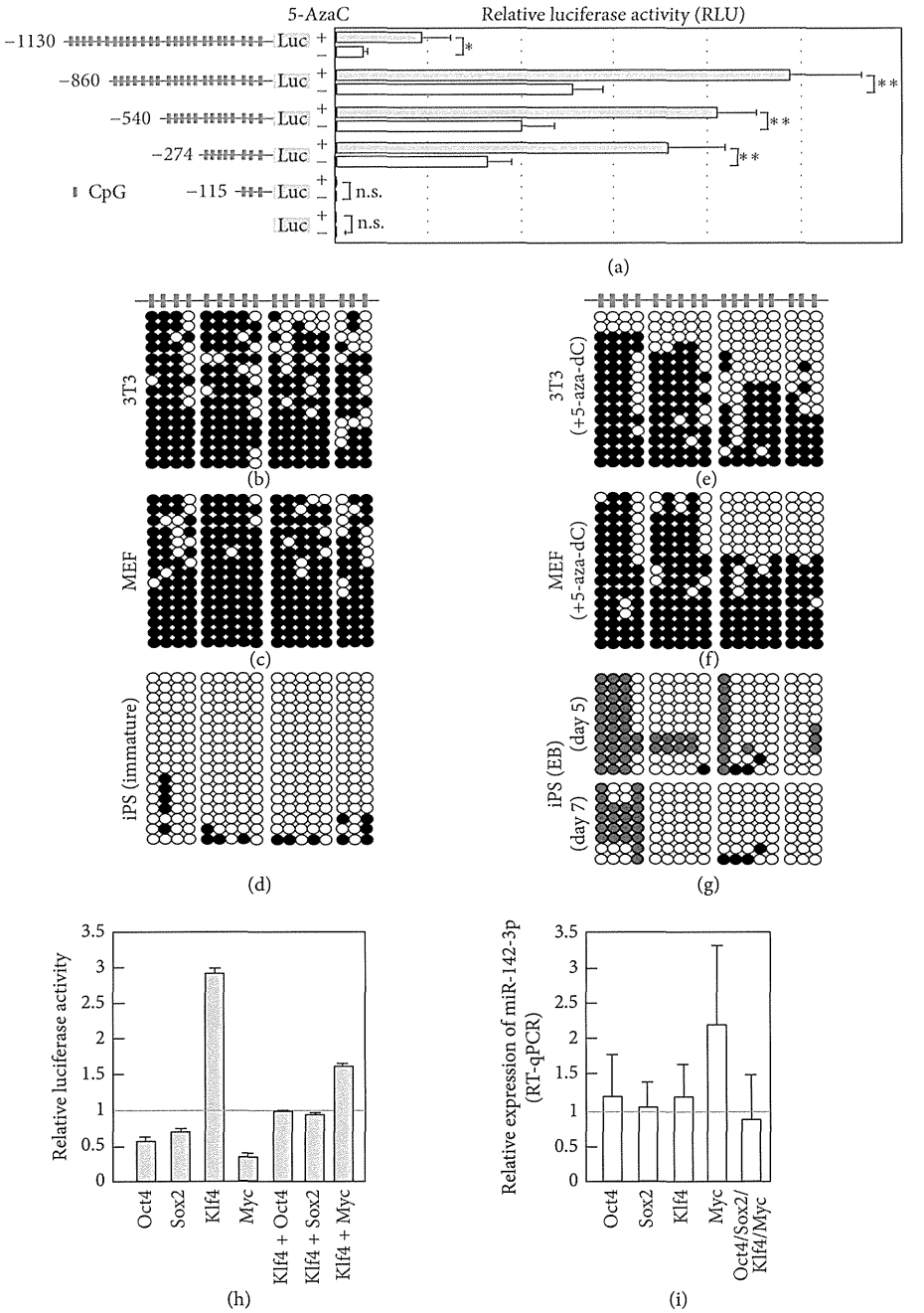

FIGURE 3: Expression of miR-142-3p was regulated by DNA methylation. (a) Left panel shows schematic representation of luciferase constructs. Luciferase analysis using plasmids containing indicated length fragments of the 5′ upstream region of miR-142-3p-luciferase was done. Plasmid was transfected into 3T3 cells, and, after 6 hours, samples were treated with DMSO or 5-aza-dC (10 μM) and cultured for additional 3 days. Then cells were harvested, and luciferase activities were examined. Values are average of 3 times independent experiments with standard deviation. P value, $** < 0.01$ and n.s. > 0.05, was calculated by Student's t-test. (b–g) CpG methylation of 5′ upstream region of miR-142-3p was examined by bisulfite conversions. Genomic DNAs extracted from 3T3, MEF in the presence or absence of 5-aza-dC, iPS, or EB prepared from iPS were subjected to bisulfite sequence. 5-Aza-dC was present in the culture medium of 3T3 or MEF 72 hours before harvesting cells for genomic DNA extraction (e, f). (h) 3T3 cells were transfected with expression plasmid of Oct4, Sox2, Klf4, or Myc with −540 Luc. For control sample, empty expression plasmid and −540 Luc were transfected. Cells were harvested after 3 days of culture, and luciferase analysis was conducted. (i) 3T3 cells were transfected with indicated expression plasmid, and, after 3 days, cells were harvested, and total RNA was extracted. Expression level of endogenous miR-142-3p was examined by RT-qPCR. (h, i) Values are relative to control vector transfected samples and average of 4 independent samples with SD.

5-aza-dC [27], suggesting that the expression of miR-142-3p was attenuated by DNA methylation not only in fibroblasts, but also in melanocyte lineage cells. In the current study, 5-aza-dC did not enhance the expression of miR-142-3p in mouse P1 thymocytes, supporting the hypothesis that DNA methylation is not a major mechanism that regulates the expression of miR-142-3p in hematopoietic cells.

The expression of miR-142-3p in hematopoietic cells is regulated by various transcription factors that also play important roles in hematopoiesis [17, 18]. The sequence of pre-miR-142 is highly conserved among vertebrates [8]. In addition, the expression of human miR-142 was recently reported to be regulated by the methylation of a CpG in its enhancer region in mesenchymal cells [8]. Although no similarity was found in the mouse and human upstream genomic regions (~2000 nt) of miR-142-3p, miR-142 expression is regulated by CpG methylation in both species.

Methylation changes occur predominantly at the end of reprogramming. The genomic region harboring pluripotency-associated genes including Nanog, Oct4, and Zfp42 is demethylated very late during reprogramming [28]. When 5-aza-dC is present during this period, an increased number of embryonic stem cell-like colonies are observed [29]. Furthermore, 5-aza-dC enhances the generation of iPS cells by inhibiting Dnmt1 activity [30]. The expression of miR-142-3p might be desilenced by the suppression of DNA demethylation and stimulated by other genes that play roles in the late phase of reprogramming. We observed that Klf4 upregulated luciferase activity but that Klf4 did not enhance the expression of endogenous miR-142-3p in 3T3 cells. Therefore, we hypothesize that a molecular environment related to reprogramming, which 3T3 cells lack, might be required for miR-142-3p expression. We identified several potential binding sites for c-Myc and Sox2 in the genomic region up to 1 kb from the miR-142 mature sequence using the Genomatix Software Suite (http://www.genomatix.de/solutions/genomatix-software-suite.html). Therefore, the combination of these transcription factors in a wider genomic region might cooperate for the full induction of miR-142-3p expression.

TGF-βR1 and TGF-βR2 were both predicted to be targets of miR-142-3p [31], and TGF-βR1 was identified as a direct target in non-small-cell lung cancer [32]. TGF-β1 is involved in the reprogramming process in which the inhibition of TGF-β signaling enhances the efficiency of reprogramming [33]. More recently, a report indicated that the miR-142-3p-mediated regulation of Wnt signaling could modulate the proliferation of mesenchymal progenitors [34]. The identification of miR-142-3p target genes in the TGF-β and Wnt signaling pathways further supports the hypothesis that miR-142-3p is involved in the regulation of iPS cell physiology.

5. Conclusions

miR-142-3p, which is highly expressed in iPS cells but not in fibroblasts, plays roles in the proliferation and differentiation of iPS cells. The expression of miR-142-3p is suppressed by DNA methylation of its CpG motifs in the 5′ genomic region in fibroblasts.

Conflict of Interests

The authors declare that there is no conflict of interests regarding the publication of this paper.

Acknowledgments

The authors acknowledge Dr. Keiko Akagawa for technical assistance and Ms. Ying Sze Tsang for initiating this project. This work is supported by a grant-in-aid from the Ministry of Education, Culture, Sports, Science, and Technology of Japan.

References

[1] G. Keller, "Embryonic stem cell differentiation: emergence of a new era in biology and medicine," *Genes & Development*, vol. 19, no. 10, pp. 1129–1155, 2005.

[2] B. E. Bernstein, T. S. Mikkelsen, X. Xie et al., "A bivalent chromatin structure marks key developmental genes in embryonic stem cells," *Cell*, vol. 125, no. 2, pp. 315–326, 2006.

[3] S. R. A. Razak, K. Ueno, N. Takayama et al., "Profiling of MicroRNA in human and mouse ES and iPS cells reveals overlapping but distinct MicroRNA expression patterns," *PLoS ONE*, vol. 8, no. 9, Article ID e73532, 2013.

[4] C.-Z. Chen and H. F. Lodish, "MicroRNAs as regulators of mammalian hematopoiesis," *Seminars in Immunology*, vol. 17, no. 2, pp. 155–165, 2005.

[5] Y. Sun, S. Varambally, C. A. Maher et al., "Targeting of microRNA-142-3p in dendritic cells regulates endotoxin-induced mortality," *Blood*, vol. 117, no. 23, pp. 6172–6183, 2011.

[6] X. S. Wang, J. N. Gong, J. Yu et al., "MicroRNA-29a and microRNA-142-3p are regulators of myeloid differentiation and acute myeloid leukemia," *Blood*, vol. 119, no. 21, pp. 4992–5004, 2012.

[7] R. Nimmo, A. Ciau-Uitz, C. Ruiz-Herguido et al., "MiR-142-3p controls the specification of definitive hemangioblasts during ontogeny," *Developmental Cell*, vol. 26, no. 3, pp. 237–249, 2013.

[8] M. Skårn, T. Barøy, E. W. Stratford, and O. Myklebost, "Epigenetic regulation and functional characterization of microRNA-142 in mesenchymal cells," *PLoS ONE*, vol. 8, no. 11, Article ID e79231, 2013.

[9] T. Nishiyama, R. Kaneda, T. Ono et al., "miR-142-3p is essential for hematopoiesis and affects cardiac cell fate in zebrafish," *Biochemical and Biophysical Research Communications*, vol. 425, no. 4, pp. 755–761, 2012.

[10] W. Hu, Y. Ye, W. Zhang, J. Wang, A. Chen, and F. Guo, "MiR-142-3p promotes osteoblast differentiation by modulating Wnt signaling," *Molecular Medicine Reports*, vol. 7, no. 2, pp. 689–693, 2013.

[11] M. K. Lalwani, M. Sharma, A. R. Singh et al., "Reverse genetics screen in Zebrafish identifies a role of miR-142a-3p in vascular development and integrity," *PLoS ONE*, vol. 7, no. 12, Article ID e52588, 2012.

[12] C. E. Gauwerky, K. Huebner, M. Isobe, P. C. Nowell, and C. M. Croce, "Activation of MYC in a masked t(8;17) translocation results in an aggressive B-cell leukemia," *Proceedings of the National Academy of Sciences of the United States of America*, vol. 86, no. 22, pp. 8867–8871, 1989.

[13] W. Kwanhian, D. Lenza, J. Alles et al., "MicroRNA-142 is mutated in about 20% of diffuse large B-cell lymphoma," *Cancer Medicine*, vol. 1, no. 2, pp. 141–155, 2012.

[14] M. Lv, X. Zhang, H. Jia et al., "An oncogenic role of miR-142-3p in human T-cell acute lymphoblastic leukemia (T-ALL) by targeting glucocorticoid receptor-α and cAMP/PKA pathways," *Leukemia*, vol. 26, no. 4, pp. 769–777, 2012.

[15] L. Wu, C. Cai, X. Wang, M. Liu, X. Li, and H. Tang, "MicroRNA-142-3p, a new regulator of RAC1, suppresses the migration and invasion of hepatocellular carcinoma cells," *FEBS Letters*, vol. 585, no. 9, pp. 1322–1330, 2011.

[16] Y. Lee, M. Kim, J. Han et al., "MicroRNA genes are transcribed by RNA polymerase II," *The EMBO Journal*, vol. 23, no. 20, pp. 4051–4060, 2004.

[17] W. Yuan, W. Sun, S. Yang et al., "Downregulation of microRNA-142 by proto-oncogene LMO2 and its co-factors," *Leukemia*, vol. 22, no. 5, pp. 1067–1071, 2008.

[18] Y. Sun, J. Sun, T. Tomomi et al., "PU.1-dependent transcriptional regulation of miR-142 contributes to its hematopoietic cell-specific expression and modulation of IL-6," *Journal of Immunology*, vol. 190, no. 8, pp. 4005–4013, 2013.

[19] N. Takayama, S. Nishimura, S. Nakamura et al., "Transient activation of c-MYC expression is critical for efficient platelet generation from human induced pluripotent stem cells," *Journal of Experimental Medicine*, vol. 207, no. 13, pp. 2817–2830, 2010.

[20] Y. Kumaki, M. Oda, and M. Okano, "QUMA: quantification tool for methylation analysis," *Nucleic Acids Research*, vol. 36, pp. W170–W175, 2008.

[21] P. H. Gunaratne, "Embryonic stem cell MicroRNAs: defining factors in induced pluripotent (iPS) and cancer (CSC) stem cells?" *Current Stem Cell Research & Therapy*, vol. 4, no. 3, pp. 168–177, 2009.

[22] B. G. Herrmann, S. Labeit, A. Poustka, T. R. King, and H. Lehrach, "Cloning of the *T* gene required in mesoderm formation in the mouse," *Nature*, vol. 343, no. 6259, pp. 617–622, 1990.

[23] G. Barreto, A. Schäfer, J. Marhold et al., "*Gadd45a* promotes epigenetic gene activation by repair-mediated DNA demethylation," *Nature*, vol. 445, no. 7128, pp. 671–675, 2007.

[24] G. Escher, A. Hoang, S. Georges et al., "Demethylation using the epigenetic modifier, 5-azacytidine, increases the efficiency of transient transfection of macrophages," *Journal of Lipid Research*, vol. 46, no. 2, pp. 356–365, 2005.

[25] L. Han, P. D. Witmer, E. Casey, D. Valle, and S. Sukumar, "DNA methylation regulates microRNA expression," *Cancer Biology and Therapy*, vol. 6, no. 8, pp. 1290–1294, 2007.

[26] M.-R. Suh, Y. Lee, J. Y. Kim et al., "Human embryonic stem cells express a unique set of microRNAs," *Developmental Biology*, vol. 270, no. 2, pp. 488–498, 2004.

[27] J. Mazar, D. Khaitan, D. DeBlasio et al., "Epigenetic regulation of microRNA genes and the role of miR-34b in cell invasion and motility in human melanoma," *PLoS ONE*, vol. 6, no. 9, Article ID e24922, 2011.

[28] J. M. Polo, E. Anderssen, R. M. Walsh et al., "A molecular roadmap of reprogramming somatic cells into iPS cells," *Cell*, vol. 151, no. 7, pp. 1617–1632, 2012.

[29] T. S. Mikkelsen, J. Hanna, X. Zhang et al., "Dissecting direct reprogramming through integrative genomic analysis," *Nature*, vol. 454, no. 7200, pp. 49–55, 2008.

[30] D. D. de Carvalho, J. S. You, and P. A. Jones, "DNA methylation and cellular reprogramming," *Trends in Cell Biology*, vol. 20, no. 10, pp. 609–617, 2010.

[31] Y. Wang, J. Gu, J. A. Roth et al., "Pathway-based serum microRNA profiling and survival in patients with advanced stage non-small cell lung cancer," *Cancer Research*, vol. 73, no. 15, pp. 4801–4809, 2013.

[32] Z. Lei, G. Xu, L. Wang et al., "MiR-142-3p represses TGF-β-induced growth inhibition through repression of TGFβR1 in non-small cell lung cancer," *The FASEB Journal*, vol. 28, no. 6, pp. 2696–2704, 2014.

[33] T. Watabe and K. Miyazono, "Roles of TGF-β family signaling in stem cell renewal and differentiation," *Cell Research*, vol. 19, no. 1, pp. 103–115, 2009.

[34] G. Carraro, A. Shrestha, J. Rostkovius et al., "miR-142-3p balances proliferation and differentiation of mesenchymal cells during lung development," *Development*, vol. 141, no. 6, pp. 1272–1281, 2014.

nature COMMUNICATIONS

ARTICLE

Received 12 May 2014 | Accepted 8 Oct 2014 | Published 24 Nov 2014

DOI: 10.1038/ncomms6514 OPEN

Pathological roles of the VEGF/SphK pathway in Niemann-Pick type C neurons

Hyun Lee[1,2,*], Jong Kil Lee[1,3,4,*], Min Hee Park[1,3,4], Yu Ri Hong[1,2], Hugo H. Marti[5], Hyongbum Kim[6], Yohei Okada[7], Makoto Otsu[8], Eul-Ju Seo[9], Jae-Hyung Park[10], Jae-Hoon Bae[10], Nozomu Okino[11], Xingxuan He[12], Edward H. Schuchman[12], Jae-sung Bae[1,3,4] & Hee Kyung Jin[1,2]

Sphingosine is a major storage compound in Niemann-Pick type C disease (NP-C), although the pathological role(s) of this accumulation have not been fully characterized. Here we found that sphingosine kinase (SphK) activity is reduced in NP-C patient fibroblasts and NP-C mouse Purkinje neurons (PNs) due to defective vascular endothelial growth factor (VEGF) levels. Sphingosine accumulation due to inactivation of VEGF/SphK pathway led to PNs loss via inhibition of autophagosome-lysosome fusion in NP-C mice. VEGF activates SphK by binding to VEGFR2, resulting in decreased sphingosine storage as well as improved PNs survival and clinical outcomes in NP-C cells and mice. We also show that induced pluripotent stem cell (iPSC)-derived human NP-C neurons are generated and the abnormalities caused by VEGF/SphK inactivity in these cells are corrected by replenishment of VEGF. Overall, these results reveal a pathogenic mechanism in NP-C neurons where defective SphK activity is due to impaired VEGF levels.

[1] Stem Cell Neuroplasticity Research Group, Kyungpook National University, Daegu 702-701, Korea. [2] Department of Laboratory Animal Medicine, Cell and Matrix Research Institute, College of Veterinary Medicine, Kyungpook National University, Daegu 702-701, Korea. [3] Department of Physiology, Cell and Matrix Research Institute, School of Medicine, Kyungpook National University, Daegu 700-842, Korea. [4] Department of Biomedical Science, BK21 Plus KNU Biomedical Convergence Program, Kyungpook National University, Daegu 700-842, Korea. [5] Institute of Physiology and Pathophysiology, University of Heidelberg, Heidelberg 69120, Germany. [6] Graduate School of Biomedical Science and Engineering/College of Medicine, Hanyang University, Seoul 133-791, Korea. [7] Department of Physiology, School of Medicine, Keio University, Tokyo 160-8582, Japan. [8] Division of Stem Cell Therapy, Center for Stem Cell Biology and Regenerative Medicine, Institute of Medical Science, University of Tokyo, Tokyo 108-8639, Japan. [9] Department of Laboratory Medicine, Asan Medical Center, University of Ulsan College of Medicine, Seoul 138-736, Korea. [10] Department of Physiology, School of Medicine, Keimyung University, Daegu 704-701, Korea. [11] Department of Bioscience and Biotechnology, Graduate School of Bioresource and Bioenvironmental Sciences, Kyushu University, Fukuoka 812-8581, Japan. [12] Department of Genetics and Genomic Sciences, Icahn School of Medicine at Mount Sinai, New York, New York 10029, USA. * These authors contributed equally to this work. Correspondence and requests for materials should be addressed to J.S.B. (email: jsbae@knu.ac.kr) or to H.K.J. (email: hkjin@knu.ac.kr).

Niemann–Pick type C disease (NP–C) is an inherited lipid storage disorder that affects the central nervous system[1–3]. Recent studies have shown that sphingosine is a major and initiating storage compound in NP–C[3,4]. However, the underlying mechanism(s) leading to sphingosine storage, as well as its role in NP–C pathogenesis such as neuronal loss, remains largely unknown.

Our previous studies have shown that bone marrow mesenchymal stem cells (BM-MSCs) contribute to improved neurological function in the NP–C mice[5,6]. Furthermore, we have postulated that the prosurvival effects of BM-MSCs on NP–C Purkinje neurons (PNs) are paracrine effects that restore the sphingolipid imbalance, as evidenced by decreased sphingosine and increased sphingosine-1-phosphate (S1P) levels[7]. Therefore, we speculated that sphingolipid-modulating factors derived from BM-MSCs are potential therapeutic agents for this disease.

Sphingolipid-metabolizing enzymes control the cellular dynamic balance of bioactive lipids, including the proapoptotic compound sphingosine and the proliferative compound S1P[8]. Sphingosine kinase (SphK) is a key enzyme that converts sphingosine into S1P. SphK can be activated by numerous external stimuli[9–12], resulting in a decrease in intracellular sphingosine and increase in S1P[13].

On the basis of these concepts and findings, we hypothesized that defects of SphK activators could be involved in the pathogenesis of NP–C, and explored candidate therapeutic factors secreted by BM-MSCs that might influence the activation of SphK. Here we show that NPC1 deficiency markedly reduces vascular endothelial growth factor (VEGF) expression, and that decreased VEGF levels cause impaired SphK activity in PNs. Abnormal sphingosine storage by VEGF-mediated SphK inactivity causes a decreased PN survival via disruption of autophagosome–lysosome fusion. Further, replenishment of VEGF leads to restoration of SphK activity and improvement of pathology by binding to the VEGF receptor-2 (VEGFR2) in NP–C mice PNs as well as patient-specific cells, preventing sphingosine accumulation, autophagy dysfunction and abnormal calcium homeostasis.

Results

SphK activity is reduced in NP–C patients and NP–C mice. We first determined whether defects of SphK could be involved in NP–C and responsible for the elevated sphingosine. SphK was significantly decreased in fibroblasts from NP–C patients compared with normal control fibroblasts (Fig. 1a). These levels did not change as the passage numbers increased (Fig. 1a). SphK activity also was decreased in the cerebellum and primary cerebellar PNs from NP–C mice compared with those of wild-type (WT) mice (Fig. 1a). These results confirmed that SphK, a key enzyme in modulating the levels of sphingosine, is diminished in NP–C, and that the reduction of this activity may influence disease progression and/or pathogenesis.

BM-MSC-derived VEGF restores SphK activity in NP–C mouse PNs. To examine whether bioactive, soluble factors released from BM-MSCs affected SphK activity in NP–C, we cocultured BM-MSCs with PNs using an indirect coculture system (see Methods). We found that when NP–C PNs were cocultured with BM-MSCs, their SphK activity was significantly increased (Fig. 1b). To identify the soluble factors that were released from the BM-MSCs and might be responsible for the increased SphK activity, we screened and compared the conditioned media (CM) of PNs grown with and without BM-MSCs using an antibody-based mouse cytokine array (Supplementary Fig. 1a,b). The CM of NP–C PNs cocultured with BM-MSCs revealed stronger signals in four array spots in comparison with the CM of NP–C PNs alone (Supplementary Fig. 1c,d). To confirm the secretion of these factors, we performed enzyme-linked immunosorbent assays (ELISA). Of the selected cytokines, only VEGF levels were significantly elevated in the CM of NP–C PNs cocultured with BM-MSCs. We also found that VEGF was significantly decreased in NP–C PNs cultured alone compared with WT PNs (Fig. 1c). To confirm these effects in PNs, we performed VEGF immunostaining. VEGF was normally expressed in PNs, but the expression levels were lower in NP–C PNs compared with WT PNs. When the NP–C PNs were cocultured with BM-MSCs, intensity of VEGF expression was increased (Fig. 1d). These data identified VEGF as a potential candidate molecule that could modulate SphK and may influence pathogenesis in NP–C PNs.

To further examine the effects of BM-MSC-derived VEGF on SphK activity in NP–C PNs, we used VEGF small interfering RNA (siRNA)-treated BM-MSCs and VEGF-overexpressing BM-MSCs (the latter derived from $VEGF^{tg}$ mice; ref. 14; Supplementary Fig. 2a). As predicted, SphK activity was significantly increased in NP–C PNs cocultured with BM-MSCs and $VEGF^{tg}$ BM-MSCs compared with NP–C PNs alone. However, the activity did not show any changes in NP–C PNs cocultured with VEGF siRNA-treated BM-MSCs (Fig. 1e). Consistent with this observation, sphingosine and S1P levels in the cocultured NP–C PNs were altered relative to the amount of VEGF released from the BM-MSCs (Supplementary Fig. 2b,c). We also performed S1P immunostaining in PNs. S1P was mainly expressed in PNs, and the expression was significantly increased in NP–C PNs cocultured with normal or $VEGF^{tg}$ BM-MSCs. However, it was not increased when the cells were cocultured with VEGF siRNA-treated BM-MSCs (Supplementary Fig. 2d).

VEGF binds to two tyrosine kinase receptors, known as VEGFR1 and 2 (ref. 15). Among these receptors, VEGFR2 is highly expressed on PNs[16]. To examine whether VEGF from BM-MSCs improved the sphingolipid imbalance in NP–C PNs by binding to VEGFR2, we treated NP–C PNs with the VEGFR2 tyrosine kinase inhibitor PTK787 before coculturing[17]. We found that SphK activity and other sphingolipid metabolites in NP–C PNs were mediated by interactions of BM-MSC-derived VEGF and its receptor VEGFR2 (Fig. 1f; Supplementary Fig. 2e). These results indicated that BM-MSC-mediated restoration of abnormal SphK activity could be due the secreted VEGF binding to the VEGFR2 in NP–C PNs.

Next, to determine whether the VEGF-mediated SphK modulation by BM-MSCs promoted the survival of NP–C PNs, we determined cell counts after coculture. When NP–C PNs were cocultured with BM-MSCs or $VEGF^{tg}$ BM-MSCs, the number of PNs was significantly increased. This effect was lower when VEGF siRNA BM-MSCs were cocultured with the NP–C PNs, although this did not reach statistical significance (Fig. 1g).

Finally, to gain more direct insights into the relationship between VEGF and SphK activity in NP–C PNs, we treated WT PNs with VEGF siRNA and determined the changes of sphingolipid factors. VEGF siRNA treatment of WT PNs strongly reduced SphK levels and led to elevation of sphingosine and reduction of S1P, similar to NP–C PNs (Fig. 1h; Supplementary Fig. 2f,g). The survival of PNs was also significantly decreased following VEGF siRNA transfection (Fig. 1i). These results suggested that inactivation of VEGF may lead to reduced SphK activity in NP–C PNs.

VEGF from BM-MSCs reduces pathology in PNs of NP–C mice. To examine the *in vivo* effects of VEGF derived from BM-MSCs on SphK activity of PNs, we transplanted BM-MSCs into the cerebellum of NP–C mice (Fig. 2a). At one day after BM-MSC

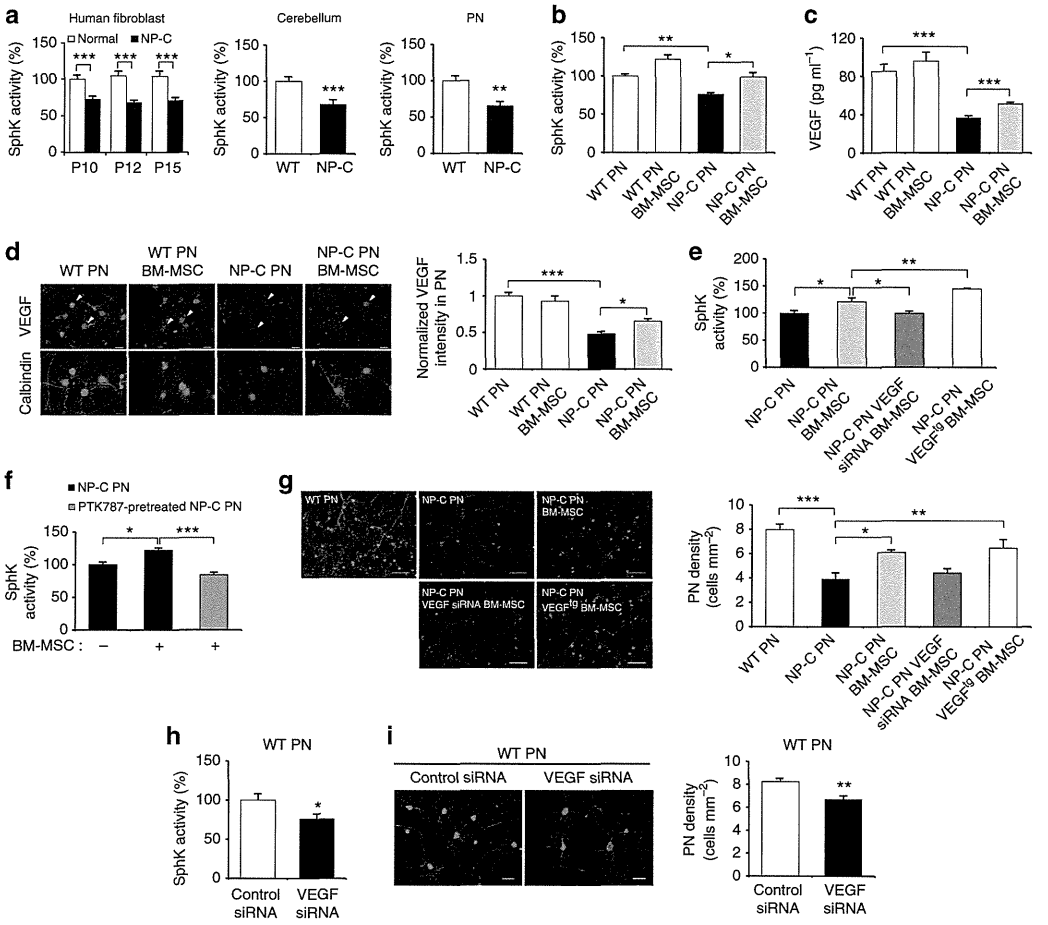

Figure 1 | BM-MSC-derived VEGF restores SphK activity in NP-C mice PNs. (**a**) SphK activities between NP-C and control were analysed in human fibroblast ($n=7$ per group), mouse cerebellum tissue ($n=7$ per group) and primary mouse PN samples ($n=9$ per group). SphK activity did not show passage differences between NP-C and normal fibroblasts. (**b**) Three days after cocultures, we measured SphK activities in PNs derived from WT and NP-C mice ($n=8$ per group). (**c**) VEGF levels were measured in CM derived from PNs with or without BM-MSCs by ELISA ($n=7$ per group). (**d**) Primary cultures of NP-C PNs were immunostained with anti-calbindin and anti-VEGF (scale bar, 50 μm). Arrowheads indicate VEGF expression by PNs. Values represent normalized fluorescence intensities of VEGF in PNs (WT PN, $n=8$; and NP-C PN, $n=9$). (**e**) SphK activities were measured in NP-C PNs alone ($n=7$) and NP-C PNs cocultured with BM-MSCs, VEGF siRNA BM-MSCs and $VEGF^{tg}$ BM-MSCs ($n=8$ per group). (**f**) Effect of the PTK787 on BM-MSCs mediated SphK activation. NP-C PNs were pretreated with PTK787 at 10 μM for 1 day and cocultured for 3 days with BM-MSCs, and then SphK activity was assayed ($n=7$ per group). (**g**) Representative images of PNs stained with anti-calbindin (scale bar, 100 μm). The mean number of PNs per squared millimetre was counted ($n=8$ per group). (**h**) Effect of VEGF knockdown on SphK activity in PNs (control, $n=6$; and VEGF siRNA, $n=8$ per group). (**i**) Representative images and quantification of neuronal survival in normal and VEGF-knockdown PNs (scale bar, 50 μm; $n=8$ per group). **a**,**h**,**i**, Student's *t*-test. **b**–**g**, one-way analysis of variance, Tukey's *post hoc* test. $^{*}P<0.05$, $^{**}P<0.01$, $^{***}P<0.005$. All error bars indicate s.e.m.

transplantation, SphK activity was significantly increased in the cerebellum of NP–C mice compared with phosphate-buffered saline (PBS)-infused counterparts (Fig. 2b). BM-MSC transplantation also increased VEGF protein levels in the cerebellum of NP–C mice (Fig. 2c). The elevated expression of VEGF was significant in the Purkinje cell layer (PCL) of the NP–C mouse cerebellums, consistent with the decreased VEGF levels in non-treated NP–C PNs compared with WT (Fig. 2d). However, BM-MSCs did not increase SphK or VEGF levels in normal cerebellums, consistent with previous reports[6,18].

We also transplanted VEGF siRNA BM-MSCs and $VEGF^{tg}$ BM-MSCs into the cerebellum of NP–C mice. As predicted, at one day after transplantation, SphK activity was significantly increased in the cerebellum of NP–C mice treated with $VEGF^{tg}$ BM-MSCs. However, mice treated with VEGF siRNA BM-MSCs showed significantly lower SphK activity (Fig. 2e). The sphingosine and S1P metabolites were also changed in NP–C PNs in relation to SphK and VEGF levels (Supplementary Fig. 3a,b). Similar effects were observed when S1P immunostaining was performed on the PN layer of NP–C mice following transplantation with VEGF siRNA or VEGF-overexpressing BM-MSCs (Supplementary Fig. 3c). To further confirm these effects, we used laser capture microdissection (LCM) to selectively isolate PNs (Supplementary Fig. 3d). We observed that expressions of *Vegf*, *VEGFR2* and *Sphk1* mRNAs were decreased in LCM-captured PNs from NP–C mice compared with that of WT mice. BM-MSC transplantation enhanced these expression levels in NP–C PNs (Fig. 2f). We also ascertained whether VEGFR2 was required for the activation of SphK in NP–C mice. As shown in Fig. 2g, SphK activity was significantly increased in the NP–C mice following BM-MSC treatment, whereas this effect was lower in NP–C mice treated with PTK787 before injecting BM-MSCs,

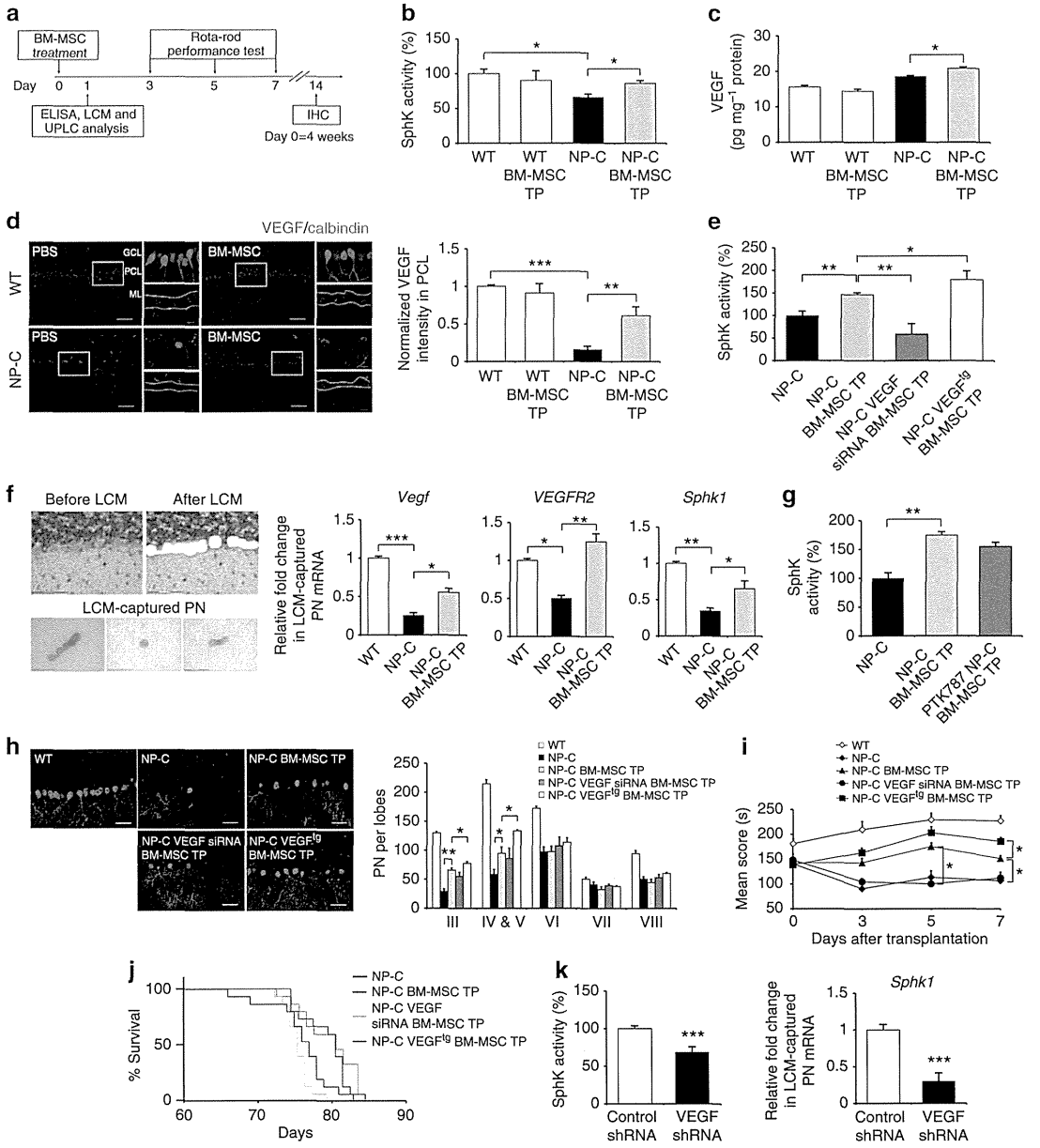

Figure 2 | VEGF from BM-MSCs reduces pathology in PNs of NP-C mice. (**a**) Protocol of BM-MSC treatment in NP-C mice. (**b**,**c**) SphK activity ($n=7$ per group; **b**) and VEGF levels ($n=8$ per group; **c**) were estimated in the cerebellums of WT and NP-C mice after BM-MSC treatment. (**d**) Cerebellar sections were stained with anti-calbindin and anti-VEGF (low-magnification scale bar, 50 μm; high-magnification scale bar, 20 μm). Values represent normalized VEGF fluorescence intensities in PCL ($n=7$ per group). (**e**) SphK activities were measured in the cerebellums of NP-C mice treated with PBS ($n=6$), BM-MSCs, VEGF siRNA BM-MSCs and $VEGF^{tg}$ BM-MSCs ($n=8$ per group). (**f**) Left, isolation of mouse PNs using LCM (scale bar, 75 μm). Right, mRNA level of *Vegf*, *VEGFR2* and *Sphk1* on LCM-captured PNs samples ($n=7$ per group). (**g**) NP-C mice were treated daily with the PTK787 at 100 mg kg^{-1} or PBS, starting 2 days before the BM-MSC transplantation. One day after BM-MSC treatment, SphK activity was estimated (NP-C, $n=7$; NP-C BM-MSC TP, $n=8$ per group). (**h**) Cerebellar sections were stained with anti-calbindin (scale bar, 50 μm), and the number of calbindin-positive PNs were quantified ($n=7$ per group). (**i**) Rota-rod scores of mice were averaged and plotted beginning 3 days after transplantation ($n=15$ per group). (**j**) Survival curve of NP-C mice ($n=15$ per group). Treatment with BM-MSCs and $VEGF^{tg}$ BM-MSCs resulted in significantly increased survival compared with PBS treatment ($P=0.0194$ and $P=0.0055$, respectively; log-rank test). (**k**) Effect of VEGF knockdown on SphK activity. Left, after intracerebellar injection of control ($n=7$) or VEGF shRNA ($n=8$) in mice, SphK activities were measured in the cerebellums. Right, relative levels of *Sphk1* mRNA from LCM-captured PNs samples ($n=7$ per group). **b**–**i**, one-way analysis of variance, Tukey's *post hoc* test. **k**, Student's *t*-test. $^{*}P<0.05$, $^{**}P<0.01$, $^{***}P<0.005$. All error bars indicate s.e.m.

although this did not reach statistical significance. S1P levels were moderately decreased with PTK787 treatment, but sphingosine did not vary between the groups (Supplementary Fig. 3e).

Next, we evaluated the effects of VEGF on the NP-C phenotype in mice. Transplantation of $VEGF^{tg}$ BM-MSCs improved NP-C pathology as measured by increased number

of calbindin-positive PNs on 14 days after treatment (Fig. 2h), and also enhanced the Rota-rod performance (Fig. 2i). These effects were less in the VEGF siRNA BM-MSC-treated group. Rota-rod performance also diminished in the VEGF siRNA BM-MSC-treated NP–C mice over time. Moreover, the lifespan of mice that had BM-MSC or VEGF^{tg} BM-MSC transplants was extended (Fig. 2j).

Finally, to determine whether the reduced VEGF levels in the cerebellums affected SphK activity, we injected VEGF short hairpin RNA (shRNA) into the cerebellum of WT mice and determined the changes of sphingolipid factors. Treatment with VEGF shRNA markedly reduced SphK activity and *Sphk1* mRNA levels (Fig. 2k; Supplementary Fig. 3f,g) and led to elevation of sphingosine and reduction of S1P (Supplementary Fig. 3h). These results suggested that inactivation of VEGF may lead to reduced SphK activity in NP–C mice, consistent with *in vitro* results. Together, these findings show a direct correlation between VEGF and SphK activity in PNs and suggest that abnormal sphingosine accumulation in NP–C may be due to the dysfunction of SphK activity by inactivated VEGF expression.

NPC1 deficiency impairs VEGF/SphK activation in PNs. We subsequently investigated the relationship between NPC1 and VEGF expression. NPC1 knockdown by siRNA markedly decreased VEGF expression in normal PNs. When NPC1 was knocked down in VEGF^{tg} PNs (derived from VEGF^{tg} mice), the decreased level of VEGF was lower than that of normal PNs (Fig. 3a–c). Moreover, NPC1 deficiency markedly inactivated SphK and led to sphingolipid imbalance. In VEGF^{tg} PNs, however, moderate changes were observed (Fig. 3d,e). We next tested whether NPC1 deficiency affected VEGF expression in the

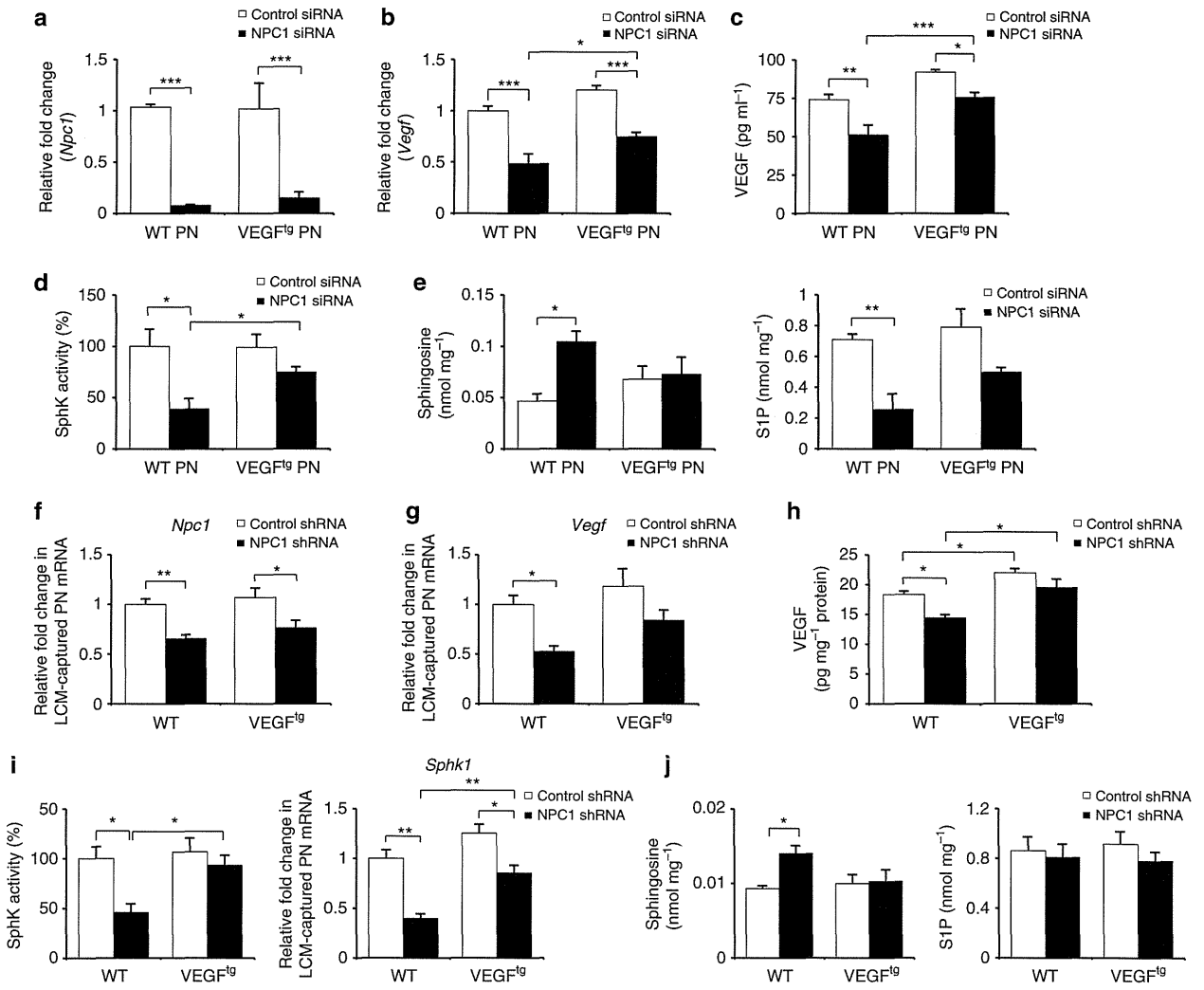

Figure 3 | NPC1 knockdown reduces VEGF expression and SphK activity. (**a–c**) Primary cultures of normal and VEGF^{tg} PNs were transfected with control or NPC1 siRNA. Three days after transfection, we measured the levels of *Npc1* (**a**) and *Vegf* (**b**) mRNA and secreted VEGF protein (**c**) in PNs ($n=7$ per group). (**d**,**e**) SphK activity (**d**), sphingosine and S1P (**e**) were estimated in PNs transfected with control ($n=6$) or NPC1 siRNA ($n=7$). (**f–j**) Four-week-old WT and VEGF^{tg} mice were injected with control or NPC1 shRNA into the cerebellum. Mice were sacrificed at 3 days after the injection. *Npc1* (**f**) and *Vegf* (**g**) mRNA levels were estimated in LCM-captured PNs and VEGF protein levels (**h**) were measured in the cerebellums ($n=7$ per group). (**i**) Left, SphK activities were measured in the cerebellums ($n=7$ per group). Right, relative levels of *Sphk1* mRNA from LCM-captured PNs samples ($n=8$ per group). (**j**) Sphingosine and S1P were measured in the cerebellums ($n=7$ per group). **a–j**, one-way analysis of variance, Tukey's *post hoc* test. $^*P<0.05$, $^{**}P<0.01$, $^{***}P<0.005$. All error bars indicate s.e.m.

cerebellums of WT mice using NPC1 shRNA. Intracerebellar injection of NPC1 shRNA, which decreased *Npc1* mRNA expression in the LCM-captured PNs (Fig. 3f), reduced VEGF expression (Fig. 3g,h). Consistently, NPC1 deficiency significantly decreased SphK activity and *Sphk1* mRNA expression and led to elevation of sphingosine and reduction of S1P in the cerebellums (Fig. 3i,j). These effects were moderated in VEGF^{tg} mice (Fig. 3g–j). Overall, these results indicated that knockdown of NPC1 may lead to reduced VEGF expression, and these reductions subsequently decreased SphK activity in PNs.

VEGF overexpression ameliorates NP-C pathology in mice. The VEGF-mediated SphK reduction in NP-C PNs prompted us to examine possible genetic implications of this pathway. To increase VEGF in NP-C mice, we generated *VEGF*^{tg}/*Npc1*$^{-/-}$ mice (Supplementary Fig. 4a). VEGF is widely expressed in neurons, glia and endothelial cells[19,20], with strong expression in PNs. In NP-C cerebellum, however, VEGF was mainly expressed in the granular layer and significantly decreased in the PCL. VEGF/NP-C mice showed increased expression of VEGF in the PCL compared with NP-C mice (Fig. 4a).

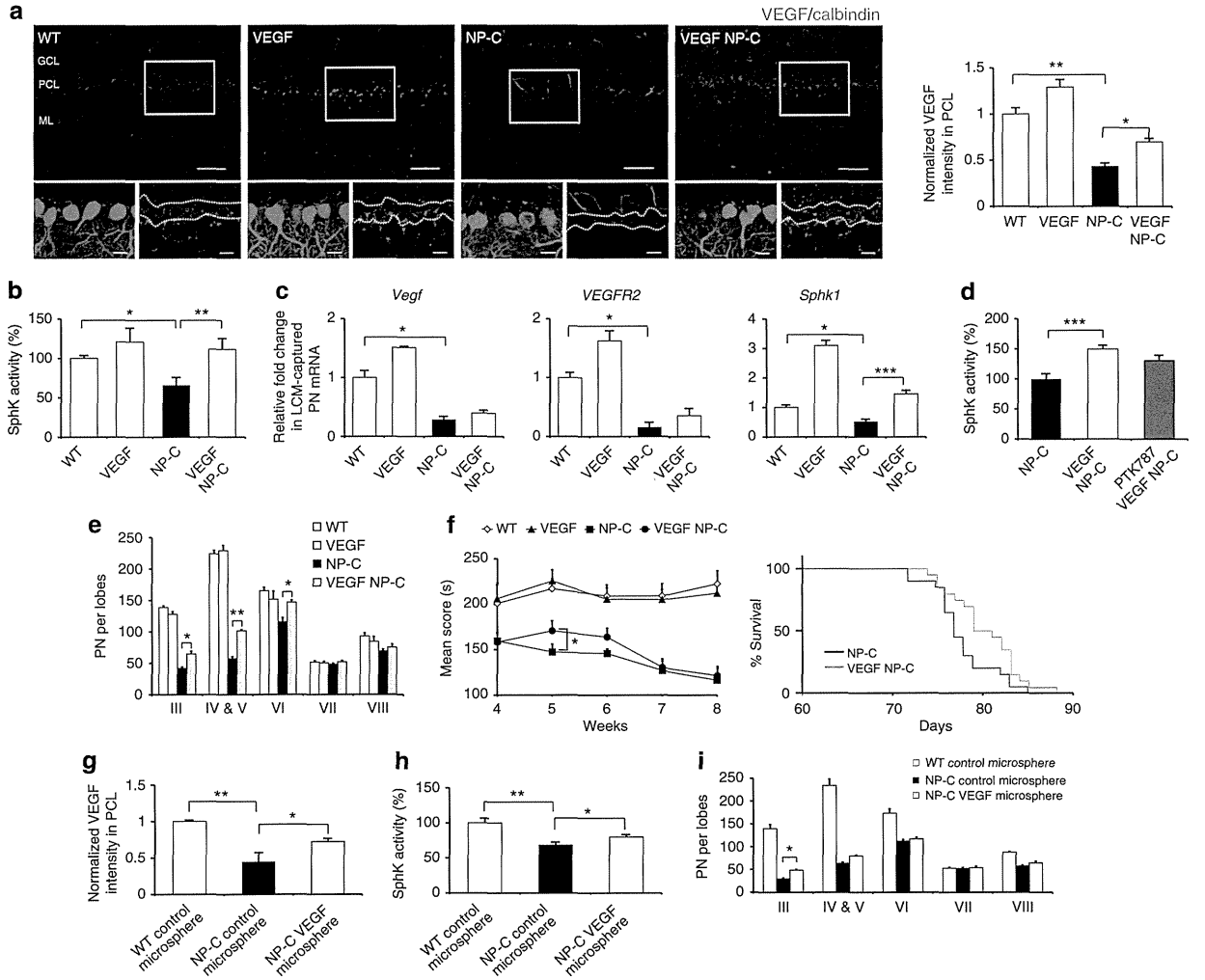

Figure 4 | Replenishment of VEGF ameliorates NP-C pathology in mice. (**a**) Cerebellar sections from 6-week-old WT, VEGF, NP-C and VEGF/NP-C mice were immunostained with anti-calbindin and anti-VEGF (low-magnification scale bar, 50 μm; high-magnification scale bar, 20 μm). The average VEGF fluorescence intensity within the PCL was measured (WT, $n=7$; VEGF, $n=7$; NP-C, $n=9$; and VEGF/NP-C, $n=9$). (**b**) SphK activities were measured in cerebellums derived from 6-week-old WT, VEGF, NP-C and VEGF/NP-C mice ($n=8$ per group). (**c**) Quantitative real-time PCR for *Vegf*, *VEGFR2* and *Sphk1* mRNA in LCM-captured PNs in 6-week-old WT, VEGF, NP-C and VEGF/NP-C mice (WT, $n=6$; VEGF, $n=6$; NP-C, $n=8$; and VEGF/NP-C, $n=8$). (**d**) VEGF/NP-C mice were treated daily with the PTK787 at 100 mg kg^{-1} or PBS vehicle control for 3 days before sacrifice (6-week-old), and SphK activity was estimated in cerebellums ($n=7$ per group). (**e**) Cerebellar sections were immunostained with anti-calbindin and the number of calbindin-positive PNs was quantified (WT, $n=7$; VEGF, $n=7$; NP-C, $n=8$; and VEGF/NP-C, $n=8$). (**f**) Left, beginning at 4 weeks of age, Rota-rod scores were averaged and plotted ($n=15$ per group). Right, survival curves of NP-C and VEGF/NP-C mice ($P=0.0548$; log-rank test, $n=15$ per group). (**g**) Cerebellar sections from WT and NP-C mice transplanted with VEGF-loaded or control microspheres were stained with anti-calbindin and anti-VEGF. The average VEGF fluorescence intensity within the PCL was measured ($n=7$ per group). (**h**) SphK activity was estimated in the cerebellums of WT and NP-C mice at one day after treatment. (**i**) Cerebellar sections were prepared at 2 weeks after transplantation and immunostained with anti-calbindin. The calbindin-positive PNs were counted ($n=7$ per group). **a–i**, one-way analysis of variance, Tukey's *post hoc* test. $^{*}P<0.05$, $^{**}P<0.01$, $^{***}P<0.005$. All error bars indicate s.e.m.

To examine whether genetically increasing VEGF affects SphK activity in NP-C PNs, we analysed cerebellum samples derived from 6-week-old WT, VEGF, NP-C and VEGF/NP-C mice. Compared with NP-C mice, VEGF/NP-C mice showed significantly increased SphK activity and decreased sphingosine accumulation (Fig. 4b; Supplementary Fig. 4b). Cerebellar S1P levels did not vary between the NP-C and VEGF/NP-C mice, although S1P levels in the PCL was increased in VEGF/NP-C mice (Supplementary Fig. 4b,d). Sphingomyelin and unesterified cholesterol levels were also significantly decreased in VEGF/NP-C mice, but glycosphingolipid (GSL) levels did not vary between the groups (Supplementary Fig. 4c,e,f). These results revealed that genetic VEGF overexpression could reverse the SphK abnormality and abnormal lipid accumulation in NP-C. To confirm VEGF-mediated SphK activation within PNs, we measured the *Vegf*, *VEGFR2* and *Sphk1* mRNA levels in LCM-captured PNs from these mice. LCM-captured PNs from VEGF/NP-C showed slightly increased *Vegf* and *VEGFR2* mRNA levels and significantly enhanced *Sphk1* mRNA levels (Fig. 4c).

Next, to further investigate the subcellular distribution pattern of SphK activity, sphingosine and S1P, we isolated cytosolic-enriched and lysosome-enriched fractions from the cerebellums. SphK activity was increased in VEGF/NP-C-derived lysosomes and cytosol compared with NP-C-derived ones, although the degree of SphK increase was greater in the cytosol than lysosome. Accumulated sphingosine in NP-C was found in the lysosome. Lysosomal sphingosine levels were significantly decreased in the VEGF/NP-C, whereas S1P levels did not vary between the groups (Supplementary Fig. 4g). Taken together, these results suggested that VEGF leads to activated SphK in the lysosome and cytosol and that activated SphK decreased lysosomal sphingosine accumulation in NP-C. We next observed whether the activation of VEGFR2 was required for the activation of SphK in VEGF/NP-C mice. Increased SphK activity was lower in VEGF/NP-C mice treated with the PTK787, although this did not reach statistical significance (Fig. 4d). Sphingosine levels also were moderately increased, but S1P levels did not vary between the groups (Supplementary Fig. 4h). PN survival was significantly improved in the VEGF/NP-C mice (Fig. 4e), and there were improvements in the Rota-rod score of 5-week-old VEGF/NP-C mice compared with NP-C mice (Fig. 4f, left). The lifespan of the VEGF/NP-C mice was slightly increased (Fig. 4f, right). We also found that BM-MSC transplantation is more effective in SphK modulation than genetic replenishment of VEGF (see Fig. 2). These results suggested that other factors secreted by BM-MSCs might also contribute to SphK activation.

We next tested whether pharmacologic delivery of recombinant VEGF is beneficial to NP-C pathology. Since the injected recombinant VEGF exerted a short-lived effect[21], to overcome this obstacle we generated a microsphere system that allows localized and sustained VEGF release (Supplementary Fig. 5a). We injected 3 mg of VEGF-loaded microspheres or control microspheres into the cerebellum of 4-week-old NP-C and WT mice. Two weeks after treatment, NP-C mice transplanted with VEGF-loaded microspheres had higher levels of VEGF expression in the PCLs (Fig. 4g), exhibited increased SphK activity (Fig. 4h) and decreased sphingosine levels (Supplementary Fig. 5b) in their cerebellums. S1P levels in cerebellum and expression in PNs were also increased by VEGF-loaded microsphere treatment (Supplementary Fig. 5b,c). Further, the VEGF-loaded microsphere-treated NP-C mice showed significantly improved PN survival (Fig. 4i).

VEGF overexpression reverses defective autophagy in NP-C mice. Autophagy, a major degradative pathway of the lysosomal system, is known to be markedly impaired in NP-C. These defects lead to loss of PNs in NP-C[22]. To examine whether increased PN survival in VEGF/NP-C mice was related to autophagy, we first measured LC3-II levels. Consistent with previous result[22], we found that the LC3-II levels were significantly increased in PNs and cerebellum samples derived from NP-C mice. This enhanced LC3-II level was reduced in VEGF/NP-C mice (Fig. 5a,b,d). The level of beclin-1 did not vary between the groups (Fig. 5a,d). The levels of cathepsin D, a lysosomal hydrolase, were slightly increased in NP-C mice compared with WT mice (Fig. 5a,d). However, the activity of cathepsin D was not changed between the groups (Fig. 5c,e). This result indicated that the elevated levels of cathepsin D in NP-C mice did not ultimately translate into a significant increase in enzyme activity. Cathepsin D levels in VEGF/NP-C mice were comparable to that of NP-C mice, indicating that increased VEGF in NP-C mice did not influence the cathepsin D expression (Fig. 5a,c–e). The level of p62 was significantly higher in NP-C mice compared with WT mice, but was decreased in VEGF/NP-C mice (Fig. 5a,d). We also performed transmission electron microscopic (EM) analysis using mouse cerebellum samples to corroborate the immunoblotting results. NP-C mice brains showed massive increases of autophagic vacuoles, while brains of VEGF/NP-C mice represented a reduced number of these vesicles (Fig. 5f).

Next, to determine whether the endocytic pathway was affected by VEGF overexpression in NP-C mice, we examined Rab5 and Rab7 expression in our animals. The levels of these proteins showed no differences between the groups (Fig. 5g). Apoptotic cells, as judged by active caspase-3, did not show any differences between NP-C and VEGF/NP-C mice (Fig. 5h). Our results showed that endocytic pathway and apoptosis were not the main mechanisms of increased PN survival in VEGF/NP-C mice.

Impaired VEGF/SphK pathway causes defective autophagic flux. Improved autophagic degradation in the VEGF/NP-C mice prompted us to analyze whether VEGF-mediated sphingolipid changes affect autophagy activity. First, to unravel the mechanistic link between VEGF levels and autophagic dysfunction, VEGF was depleted in the WT PNs by siRNA treatment. Knockdown of VEGF caused increased accumulation of LC3-II and p62 (Fig. 6a,b). Beclin-1 expression was not affected by VEGF knockdown (Fig. 6a), indicating that the accumulation of autophagosomes was not due to the biogenesis pathway.

The accumulation of autophagosomes can occur due to either an increase in their rate of formation or a reduction in their rate of degradation[23]. To distinguish between these two events, we examined the effects of VEGF knockdown on LC3-II levels in WT PNs in the presence or absence of NH_4Cl that blocks autophagic degradation but does not affect autophagosome formation. VEGF knockdown increased accumulation of LC3-II. This level was not further increased by NH_4Cl treatment (Fig. 6c, left). In contrast, VEGF depletion in serum starvation culture resulted in a significant increase in LC3-II levels (Fig. 6c, right). These observations were also supported by levels of p62 (Fig. 6c). These results suggested that VEGF depletion influences at a late step of autophagy. We also performed autophagy flux assay in WT, NP-C and VEGF/NP-C mice PNs. Under basal condition, NP-C PNs showed significantly increased LC3-II and p62 levels compared with WT PNs. NH_4Cl-induced lysosome inhibition led to marked increase of LC3-II and p62 levels in the WT PNs, but this increase was significantly less in the NP-C PNs (Fig. 6d). VEGF/NP-C PNs showed similar pattern in LC3-II and p62 increase compared with WT cells (Fig. 6d). Taken together, these

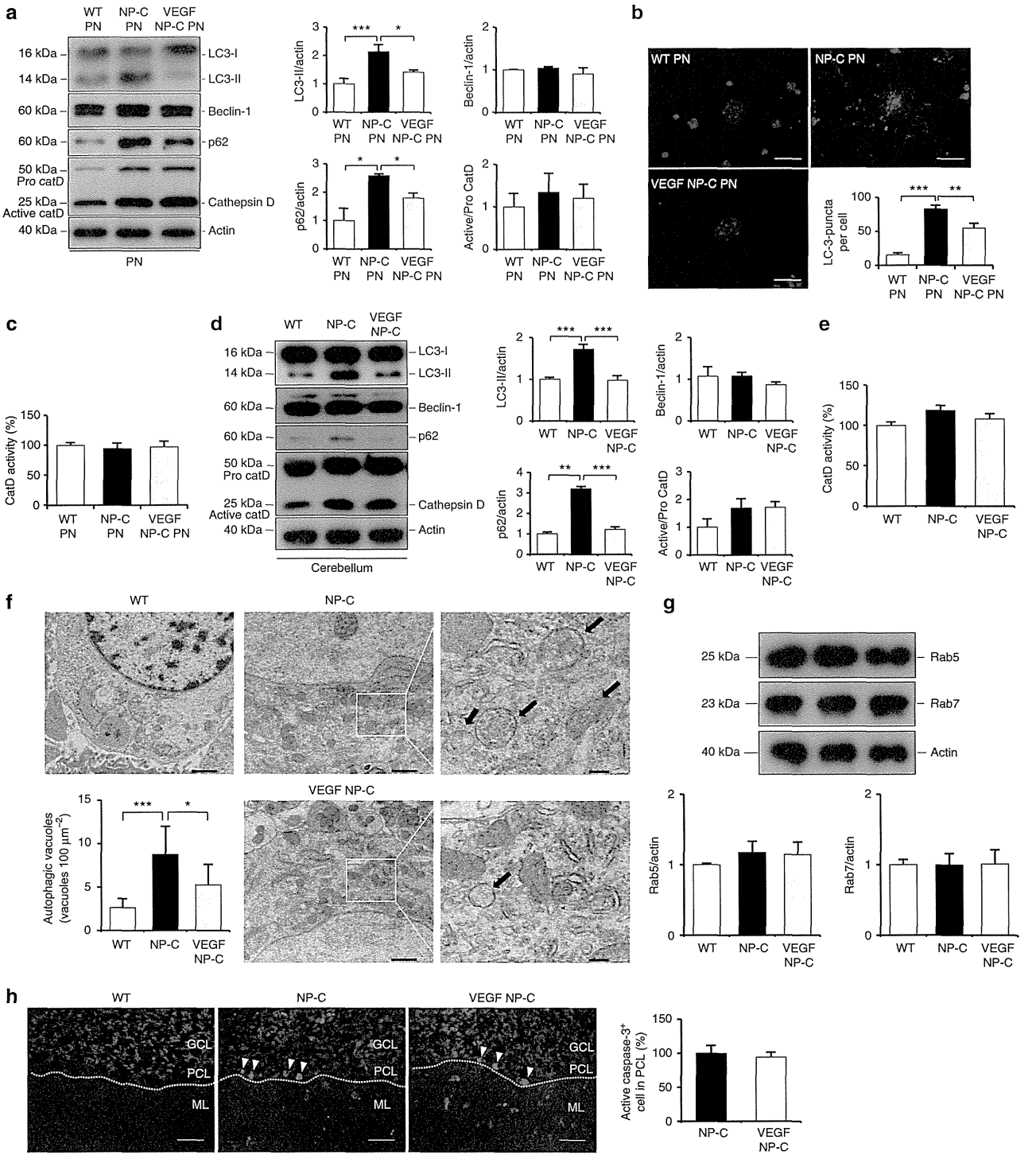

Figure 5 | VEGF replenishment reverses defective autophagy in NP-C mice. (**a**) Western blot analysis of LC3, beclin-1, p62 and cathepsin D in primary cultured PNs derived from WT, NP-C and VEGF/NP-C mice (WT, $n=5$; NP-C, $n=6$; and VEGF/NP-C, $n=6$). (**b**) Immunocytochemistry of LC3 in WT, NP-C and VEGF/NP-C PNs ($n=6$ per group; scale bar, 20 μm). (**c**) Cathepsin D activity in primary cultured PNs (WT, $n=5$; NP-C, $n=6$; and VEGF/NP-C, $n=6$). (**d**) Western blot analysis of LC3, beclin-1, p62 and cathepsin D in the cerebellums of 6-week-old WT, NP-C and VEGF/NP-C mice (WT, $n=6$; NP-C, $n=7$; and VEGF/NP-C, $n=7$). (**e**) Cathepsin D activity in the cerebellums of WT, NP-C and VEGF/NP-C mice (WT, $n=5$; NP-C, $n=6$; and VEGF/NP-C, $n=6$). (**f**) EM images and quantification data of the cerebellum ($n=5$ per group; low-magnification scale bar, 1 μm; high-magnification scale bar, 200 nm). Arrow indicates autophagic vacuole. (**g**) Western blot analysis of Rab5 and Rab7 levels in the cerebellum ($n=6$ per group). (**h**) Cerebellar sections were immunostained with anti-active caspase-3 and the number of active caspase-3-positive cells in PCL was quantified ($n=5$ per group; scale bar, 50 μm). **a**–**g**, one-way analysis of variance, Tukey's *post hoc* test. **h**, Student's *t*-test. $^{*}P<0.05$, $^{**}P<0.01$, $^{***}P<0.005$. All error bars indicate s.e.m.

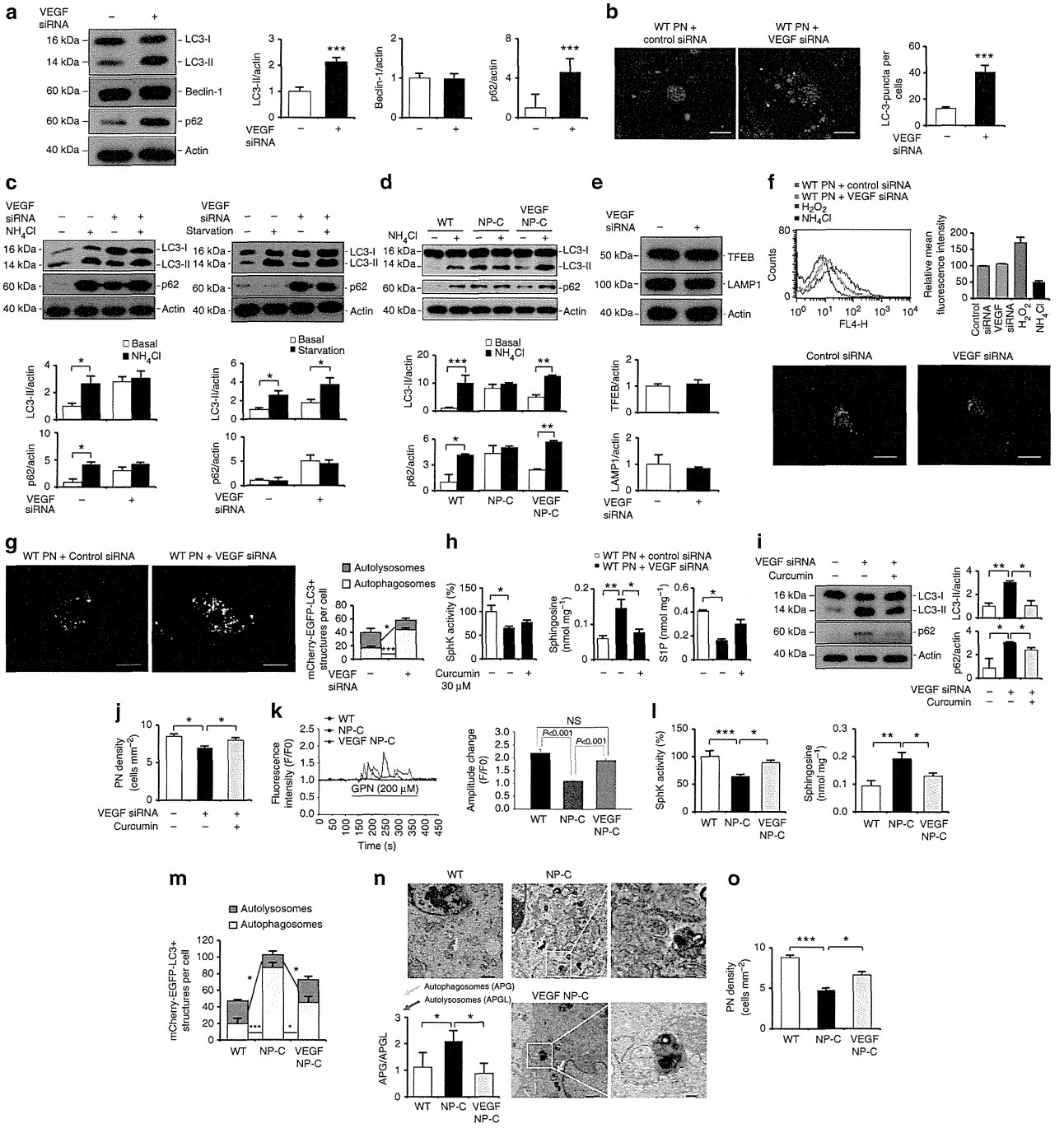

Figure 6 | VEGF/SphK inactivity impairs autophagic flux. (**a**) Western blots of LC3, beclin-1 and p62 in PNs after VEGF knockdown ($n=6$ per group). (**b**) Immunocytochemistry of LC3 in PNs after VEGF knockdown ($n=6$ per group; scale bar, 20 μm). (**c**) Autophagic flux assay. Western blots of LC3 and p62 in PNs ($n=6$ per group). (**d**) Western blots of LC3 and p62 in cultured PNs in the presence of NH_4Cl ($n=5$ per group). (**e**) Western blots of TFEB and Lamp1 in VEGF-knockdown PNs (control, $n=5$ and VEGF siRNA, $n=6$). (**f**) Effect of VEGF knockdown on lysosomal pH. PNs stained with LysoTracker red ($n=5$ per group; scale bar, 20 μm). (**g**) Fluorescence analysis of autophagosomes and autolysosomes (control, $n=7$ and VEGF siRNA, $n=8$; scale bar, 10 μm). (**h**) Sphk activity, sphingosine and S1P levels in PNs after VEGF knockdown in the presence of curcumin ($n=8$ per group). (**i**) Western blot analysis of LC3 and p62 in VEGF-knockdown PNs treated with curcumin (control, $n=7$; VEGF siRNA, $n=8$; and VEGF siRNA/curcumin, $n=8$). (**j**) Survival of VEGF-knockdown PNs treated with curcumin ($n=8$ per group). (**k**) Left, representative traces showing intracellular $[Ca^{2+}]$ changes monitored in single fluo-4-loaded PNs. Right, maximal peak fluorescence changes were determined as the differences between basal and the maximum fluorescence ($n=10$ cells per group). (**l**) Sphk activity and sphingosine levels were measured in cultured PNs ($n=8$ per group). (**m**) Quantification of autophagosomes and autolysosomes in primary cultured PNs (WT, $n=7$; NP-C, $n=7$; and VEGF/NP-C, $n=8$). (**n**) EM analysis of the PNs ($n=5$ per group; low-magnification scale bar, 1 μm; high-magnification scale bar, 200 nm). (**o**) Survival of primary cultured PNs (WT, $n=6$; NP-C, $n=8$; and VEGF/NP-C, $n=8$). **a**,**b**,**e**,**g**, Student's *t*-test. **c**,**d**,**f**,**h**–**o**, one-way analysis of variance, Tukey's *post hoc* test. $^*P<0.05$, $^{**}P<0.01$, $^{***}P<0.005$. All error bars indicate s.e.m.